Diploma Thesis

Velocity and Acceleration Measurements on the Casing of Hydraulic Laboratory Models

Written for the purpose of obtaining the academic degree of

DIPLOM-INGENIEUR

under the supervision of

Univ.Prof. Dipl.-Ing. Dr.-Ing. Christian BAUER
Ass.Prof. Dipl.-Ing. Dr.techn. Eduard DOUJAK

submitted at the Vienna University of Technology

Faculty of Mechanical and Industrial Engineering

by

Markus EICHHORN
Matr.Nr. 0525514
Obritz 233, A-2061 Hadres

Vienna, January 2013

.....
(Markus Eichhorn)

Erklärung

Ich erkläre hiermit an Eides statt, dass ich meine Diplomarbeit nach den anerkannten Grundsätzen für wissenschaftliche Abhandlungen selbstständig ausgeführt habe und alle verwendeten Hilfsmittel, insbesondere die zugrunde gelegte Literatur genannt habe.

Weiters erkläre ich, dass ich dieses Diplomarbeitsthema bisher weder im In- noch im Ausland (einer Beurteilerin/einem Beurteiler zur Begutachtung) in irgendeiner Form als Prüfungsarbeit vorgelegt habe und dass diese Arbeit mit der vom Begutachter beurteilten Arbeit übereinstimmt.

Vienna, January 2013 .....

(Markus Eichhorn)

Vorwort

Ich bedanke mich bei Univ.Prof. Dipl.-Ing. Dr.-Ing. Christian Bauer und Ass.Prof. Dipl.-Ing. Dr.techn. Eduard Doujak für die hervorragende Betreuung bei der Durchführung dieser Diplomarbeit. Weiters bedanke ich mich bei der Firma *Brüel & Kjaer Vibro* für die Bereitstellung aller benötigten Hilfsmittel und die finanzielle Unterstützung. Ein besonderer Dank gilt hierbei Herrn Peter Surland M.Sc.EE und Dipl.-Ing. Alfred Schübl, die mich mit dem nötigen fachlichen Wissen versorgt haben.

An dieser Stelle möchte ich mich ausdrücklich bei meiner Familie bedanken, die mich während meiner Studienzeit bestmöglich unterstützt und mein Studium erst ermöglicht hat.

Abstract

The aggregate phases of water and other fluids depend not only on the temperature but also on the static pressure, leading to the phenomena called cavitation in hydraulic machinery. Flow acceleration in impellers of pumps and turbines induces a drop of pressure and as consequence a part of the fluid is vaporised even at constant temperature. The release of steam bubbles results in a two-phase flow, which decrements the efficiency of the hydraulic machine and the total head especially of pumps. Further the sudden implosion of bubbles in regions of higher pressure causes material erosion damages on affected component surfaces and vibration and noise in the machinery. Due to the fact, that cavitation cannot be avoided completely in pumps and especially in turbines of hydropower plants, special detection methods have to be developed and improved, to keep the negative impacts in an acceptable range. The investigations performed for this diploma thesis at the Vienna University of Technology with kind support of the company *Brüel & Kjaer Vibro* deal with vibration and acceleration measurements on the casing of a laboratory model. It consists of a radial pump system, where the cavitation processes can be exactly simulated, to correlate the detected vibration signals to the cavitation intensity. Pressure and flow transducers and visual documentations of the processes inside the pump help verifying the vibration measurements. The results achieved should finally help to develop a cavitation monitoring system.

Kurzfassung

Die Aggregatszustände von Wasser und anderen Fluiden hängen nicht nur von der Temperatur, sondern auch vom statischen Druck ab, was in hydraulischen Maschinen zu dem sogenannten Phänomen der Kavitation führen kann. Eine Beschleunigung der Strömung in den Laufrädern von Pumpen und Turbinen bewirkt einen Druckabfall, wodurch ein Teil des Fluids auch bei konstanter Temperatur verdampft. Die Freisetzung von Dampfblasen resultiert in einer Zwei-Phasen-Strömung, welche einen Abfall des Wirkungsgrades in hydraulischen Anlagen und der Förderhöhe speziell bei Pumpen bewirkt. Desweiteren verursachen die plötzlichen Implosionen der Blasen in Zonen höheren Druckes Erosionsschäden an den Oberflächen betroffener Bauteile und Schwingungen und Lärm an der Maschine. Aufgrund der Tatsache, dass Kavitation in Pumpen und speziell in Turbinen von Wasserkraftwerken nicht gänzlich vermieden werden kann, ist es notwendig spezielle Messsysteme zu entwickeln und zu verbessern, um die negativen Auswirkungen in akzeptablen Grenzen zu halten. Die Untersuchungen, welche im Zuge dieser Diplomarbeit an der Technischen Universität Wien mit freundlicher Unterstützung der Firma *Brüel & Kjaer Vibro* durchgeführt wurden, behandeln Schwingungs- und Beschleunigungsmessungen am Gehäuse eines Labormodells. Dieses besteht aus einem Radialpumpensystem, an dem die Kavitationsvorgänge genau simuliert werden können, um die erfassten Schwingungssignale mit der Kavitationsintensität in Verbindung bringen zu können. Druck- und Durchflussmessungen und eine visuelle Dokumentation der Vorgänge in der Pumpe tragen zusätzlich zur Verifizierung der Vibrationsmessungen bei. Die erzielten Resultate sollen letztendlich zur Entwicklung eines Kavitationsüberwachungssystems beitragen.

Contents

Symbols and Definitions

Symbol	Definition	Unit
A	area, cross section	m^2
b	number of impeller blades	-
c	absolute velocity	m/s
c_{1m}	meridional component of absolute velocity	m/s
c_{1u}	circumferential component of absolute velocity	m/s
d	diameter	m
E_{Rs}	losses in pipelines	m^2/s^2
f	frequency	Hz
g	acceleration due to gravity	m/s^2
H	total head	m
h	height	m
i_1	incidence angle	$^\circ$
l	length	m
n	rotational speed	min^{-1}
n_q	specific speed	min^{-1}
NPSH	net positive suction head	m
$NPSH_A$	net positive suction head available	m
$NPSH_i$	net positive suction head for cavitation inception	m
$NPSH_R$	net positive suction head required	m
$NPSH_x$	net positive suction head with x-percent drop of head	m
p	static pressure	bar
Q	flow rate	m^3/h
Q_{Im}	flow rate through impeller	m^3/h
RMS	root mean square	
T	temperature	$^\circ C$
u_1	circumferential velocity	m/s
z	height difference	m

Greek Letters

Symbol	Definition	Unit
α	angle between absolute and circumferential velocity	$^\circ$
β_1	flow angle	$^\circ$
β_{1B}	blade angle	$^\circ$
ζ	loss coefficient	-
η_l	leakage factor	-
λ	friction coefficient for pipelines	-
ν	fluid viscosity	m^2/s
ρ	density	kg/m^3
σ	cavitation coefficient	-

Subscripts

Symbol	Definition
1	impeller inlet
e	tank
Im	impeller
min	minimum
n	impeller hub
opt	optimum
p	outlet
PS	pressure side
s	inlet
SF	shock-free
SS	suction side
stat	static
v	vapour

1 Introduction

Fluid flow machinery and especially hydraulic machines occupy an important role in human's life. The use of hydropower and its transformation from potential in mechanical energy supported the social and economic evolution of mankind a long time ago. The modern energy supply and storage is based on a more or less considerable degree of hydropower plants, which gain increasing significance due to climatic changes caused by fossil energy sources and a rising rejection of nuclear power plants in society. The transport of liquid fluids, especially the supply of water, is connected to several techniques of pumping devices, which nowadays occur in a large number of applications in the industry and in our daily life.

The majority of pumps and all types of hydraulic turbines are working with rotating impellers, which are responsible for the transformation from mechanical to potential energy (pumps) or reverse (turbines). While the physical fundamentals of fluid mechanics in hydraulic machines are well known, several phenomena exist, whose reasons, effects and metrological acquisitions are not yet clarified completely. One of these phenomena is the so called cavitation, which describes the appearance of steam bubbles in the fluid flow at nearly constant temperature due to a drop of static pressure (see Chap. 2). Affected from this phenomena are reaction turbines (Francis and Kaplan turbines), axial and radial pumps, but also propeller of ships, where the fluid pressure changes during the flow through the impeller. Due to the implosion of the induced steam bubbles in regions with a higher static pressure, pressure pulsations are generated, which can cause damages in machinery components. Since also noise and vibrations are generated, they can be used to determine the cavitation intensity by developing different detection systems.

In collaboration with the company *Brüel & Kjaer Vibro*, which has focused on monitoring systems especially for hydropower plants, investigations with different vibration sensors and further measurement techniques are accomplished on a laboratory test rig (see Chap. 4). The laboratory model, consisting primary of a radial pump

with an impeller diameter of approximately 300 mm, is set up in the hydrodynamic laboratory at the Vienna University of Technology. Most of the measurement equipment is provided by *Brüel & Kjaer Vibro*. The purpose of the investigations and the diploma theses is the development of a cavitation monitoring system by using acceleration sensors mounted on the pump casing, to quantify the cavitation intensity.

Many studies already exist related to cavitation and its impact on hydraulic machinery. Boorsma and Fitzsimmons [6] investigated the propagation of cavitation induced noise on a ship's propeller through the shaft, to detect the cavitation intensity by using shaft-mounted acoustic emission transducers. Bajic [3, 4] developed a multidimensional diagnostic system with a large number of hydrophones, pressure transducers and vibro-acoustic sensors, which enables a temporal and spatial resolution of the cavitation processes. Lang, Dimitrov and Pelz [7] developed a new pressure sensor technique, by using a thin PVDF (polyvinylidene fluoride) membrane with a matrix-structure, also to resolve the steam bubble implosions in a spatial way. Other studies approach the thematic of cavitation erosion. Keil, Pelz, Cordes and Ludwig [9] developed an automatic pit-count measurement system at the *TU Darmstadt*, to quantify appearing erosion damages. A brief description of the current state of the measurement techniques is given in Chap. 3.

2 Fundamentals of Cavitation

2.1 Physical Basics

The three phases of water - solid, liquid and gaseous - can be described in a p-T diagram (see Fig. 2.1). Water can be vaporised from its liquid state by increasing the temperature at constant pressure or by decreasing the pressure at constant temperature.

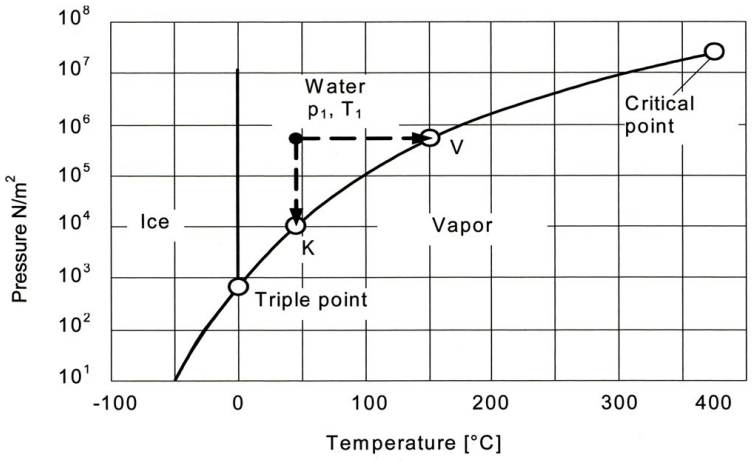

Figure 2.1: Phase equilibrium of water [1]

Cavitation in a flow through system occurs when a small part of the fluid is vaporised due to the static pressure drop into the range of the temperature dependent vapour pressure of the fluid in consequence of flow-acceleration (e.g. in a nozzle or in the runner of a radial pump). As a result steam bubbles are developed at approximately constant temperature, which are carried along with the flow - a localized two-phase flow occurs. As soon as the steam reaches an area, where the static pressure exceeds the saturation pressure (e.g. by decelerating the flow), it is condensed and collapses in an implosive way.

The flow acceleration and deceleration can be described in a venturi nozzle (see Fig. 2.2): The pressure in front of the nozzle, where the flow is not interfered, is $p_{0,stat}$. When the flow reaches the nozzle the cross section is reduced to A_1 and the pressure decreases in consequence of the acceleration to p_{min}. Depending on the fluid temperature the saturation pressure varies from $p_{v,1}$ to $p_{v,4}$. If the pressure p_{min} is lower than the saturation pressure the first steam bubbles will occur. Downstream of the nozzle the cross section is increasing and the static pressure is enhanced to $p_{2,stat}$. Depending on the saturation pressure the phase equilibrium is impaired and the bubbles will condense immediately.

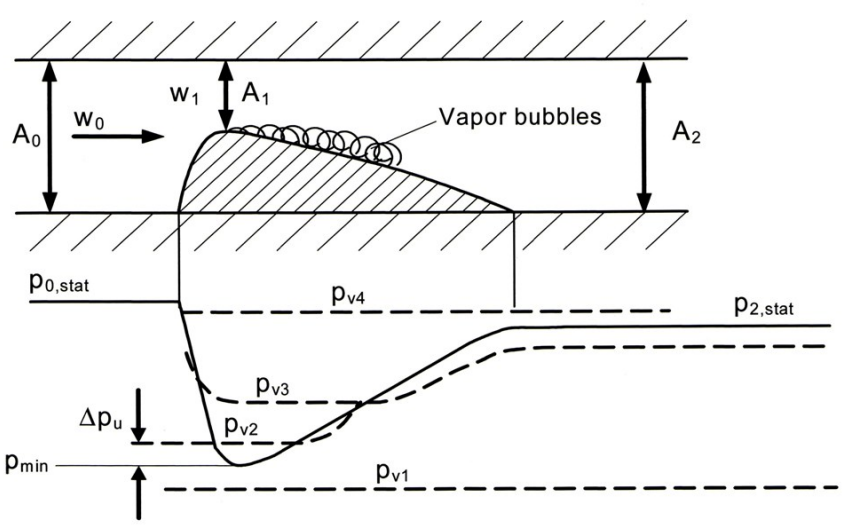

Figure 2.2: Cavitation in a nozzle [1]

As a result the pressure inside the bubbles drops and the bubbles collapse because of the higher ambient pressure. Two cases of collapses have to be distinguished:

1. Spherically symmetrical collaps without any pressure gradient (see Fig. 2.3a)

2. Asymmetrical collaps evoked by a pressure gradient or in proximity to a solid surface (see Fig. 2.3b and c). This type of collapse mostly appears in technical flows. Due to the high collapsing velocities a so called “micro-jet” occurs with pressure peaks of more than 1000 bar, which can exceed the strength of the used materials.

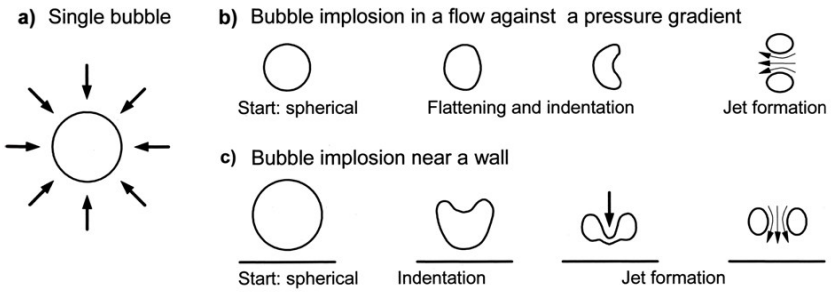

Figure 2.3: Bubble implosion [1]

To have an impact on material surfaces the implosions have to occur very close to them because the diameter of the micro-jet is in the range of one-tenth millimetre. If the cavitation exposure on the surface is long enough material removal and erosion damage can occur on affected components, depending on the cavitation intensity and the used material. The damages can range from a small amount of micro-pitting after a long operational time to destructive failures of whole components, which entails expensive maintenance. Especially the runner blades and guide vanes of pumps and turbines are affected.

Another consequence of cavitation is a constriction of the cross-section due to an appearing two-phase flow. As a result the discharge and the efficiency of pumps and turbines and the total head of radial pumps decreases.

Due to the growth and implosion of the steam bubbles, pressure waves are generated which create noise and vibrations through the fluid and the mechanical structures. The intensity and the frequency range of the vibrations can be used to determine the strength of cavitation, which is declared in section 2.4.

2.2 Cavitation in Hydraulic Machinery

The energy transfer in pumps or turbines takes place by a redirection of the flow between the curved blades of the rotating impeller. In radial pumps the fluid is decelerated which causes an increase of the static pressure and enables the fluid transport. In turbines the fluid's pressure energy is transferred to kinetic energy in the impeller by acceleration.

The flow around the runner blades of a fluid-flow machine can be compared to

the flow around an air foil, where the pressure on the suction side p_{SS} (upper wing surface) is smaller than the ambient pressure p_0 and the pressure on the pressure side p_{PS} (lower wing surface) is bigger than p_0 (see Fig. 2.4).

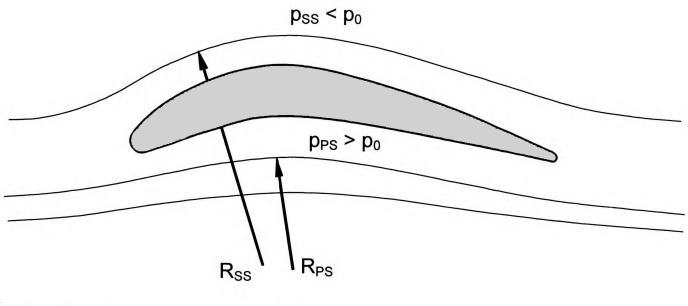

Figure 2.4: Flow around an air foil [1]

The inflow of the runner blade and the pressure distribution is shown in Fig. 2.5: The static pressure p_s in the inlet structure drops to p_1 at the leading edge due to flow losses and than drops to the minimum pressure p_{min} on the blade suction side due to the flow around the profile right behind the leading edge. If the pressure p_{min} is beneath the saturation pressure p_v cavitation bubbles will appear. Downstream the blade the pressure on the suction side increases again and the occurring cavitation bubbles collapse. The length of the bubble-area (cavity) increases with the length of the zone where $p_{min} < p_v$.

The pressure distribution of the hydrofoil is not only depending on its profile but also on the flow angle β_1 and on the blade angle β_{1B}. The flow angle itself is varying with the velocity conditions at the runner entry and therefore depending on the flow rate and the rotational speed of the runner. The velocity triangles, the angles at the blade entry and the runner geometry are shown in Fig. 2.6. The relation for the flow angle is

$$\beta_1 = \arctan \frac{c_{1m}}{u_1 - c_{1u}} \tag{2.1}$$

with the meridional component of the absolute velocity c_{1m}, the circumferential component of the absolute velocity c_{1u} and the circumferential velocity u_1. The velocity c_{1u} can be calculated with the angle α between the absolute velocity c_1 and c_{1u} by

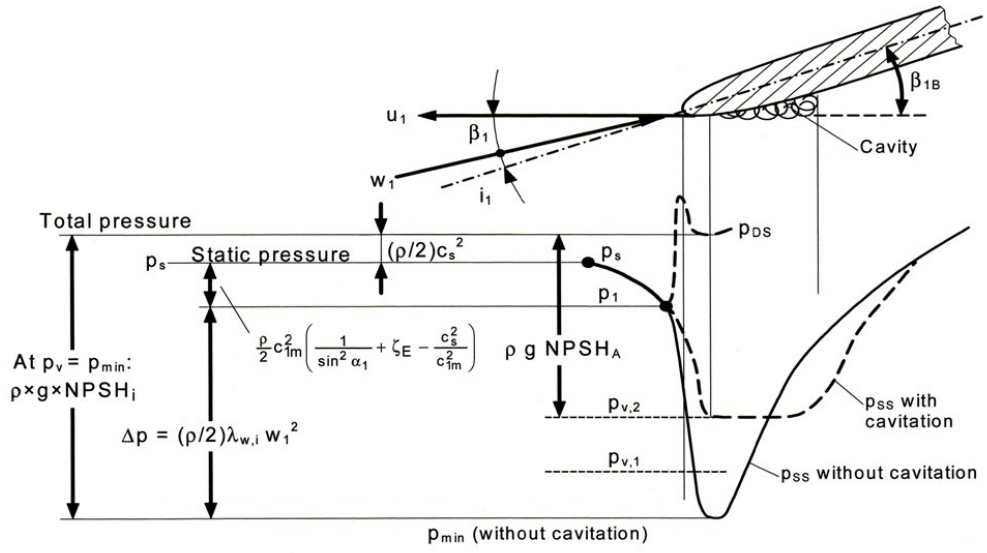

Figure 2.5: Cavitation on the leading edge of a runner blade [1]

$$c_{1u} = \frac{c_{1m}}{\tan \alpha} \tag{2.2}$$

The circumferential velocity is calculated with the revolutions per minute n and the inlet diameter d_1 by

$$u_1 = \frac{\pi d_1 n}{60} \tag{2.3}$$

If the fluid flows in axial direction to the runner entry, the circumferential component is $c_{1u} = 0$ because $\alpha = 90°$. The meridian component is calculated by

$$c_{1m} = \frac{Q_{Im}}{A_1} = \frac{4Q_{Im}}{\pi(d_1^2 - d_n^2)} \tag{2.4}$$

with the flow rate through the impeller Q_{Im}, consisting of the available flow rate Q and the leakage through the runner sealings, and the crossflow section A_1 of the runner, which is calculated by the appropriate diameters of the runner. The simplified calculation of the crossflow section by the inlet diameter d_1 and the hub diameter d_n is only valid, if the specific speed n_q of the pump is in the lower range. For higher values of n_q the crossflow section at the inlet of the pump differs from an annulus cross section and has therefore to be calculated more detailed. The calculation of the

specific speed for the used pump will be shown in section 5.1.

The difference between the blade angle and the flow angle is the incidence angle:

$$i_1 = \beta_{1B} - \beta_1 \tag{2.5}$$

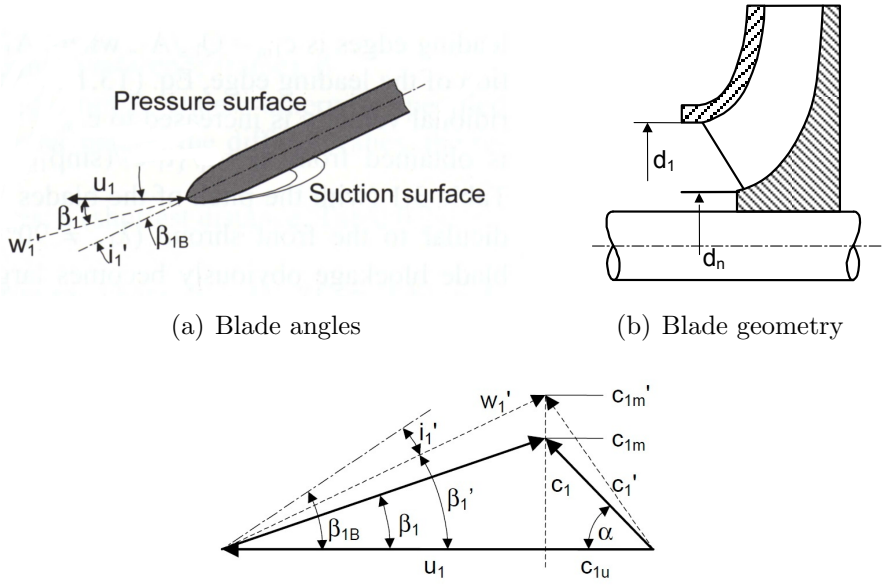

(a) Blade angles

(b) Blade geometry

(c) Velocity triangles

Figure 2.6: Incidence angle [1]

If the incidence angle is $i_1 \geq 0$ the pressure on the suction side is much lower than on the pressure side of the blade and possible cavitation bubbles will occur on the suction side. In the case of $i_1 < 0$ the stagnation point appears on the suction side and the pressure on the blade's pressure side behind the leading edge is lower than on the suction side. Due to this cavitation will appear on the pressure side of the runner (see Fig. 2.7): The dimensionless pressure coefficient c_p is defined as

$$c_p = \frac{p - p_\infty}{\frac{1}{2}\rho_\infty c_\infty^2} \tag{2.6}$$

with the measured pressure p at a specific point, the static pressure in the inflow p_∞, the density of the fluid ρ_∞ and the velocity of the fluid in the inflow c_∞.

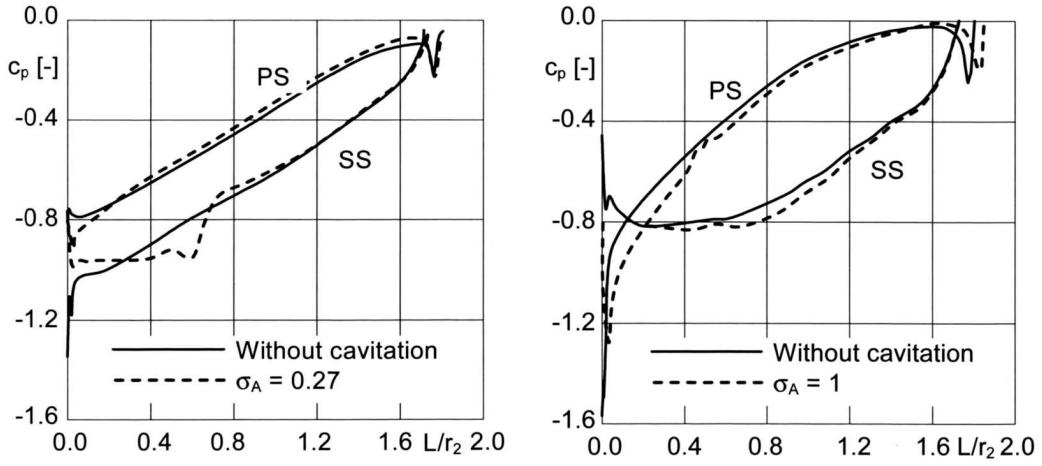

(a) $i = 5°$ (b) $i = -12°$

Figure 2.7: Pressure distribution depending on the incidence angle [1]

The calculation of the incidence angle depending on the flow rate for the used pump will be shown in section 5.1.

2.3 Cavitation Criteria

The most significant factor for the appearance of cavitation in the runner of a pump or turbine is the minimum static pressure p_{min} at the runner's leading edge (pump) or trailing edge (turbine) as mentioned above. Due to the fact that this value is not easy to measure, several coefficients like the cavitation number σ or the NPSH value exist, which describe the cavitation state using the static pressure and the flow velocity on the suction side and the vapour pressure of the fluid. The NPSH value ("Net Positive Suction Head") can be described as the difference between the absolute energy head at the pump's entry and the vapour pressure height (see Fig. 2.8):

$$NPSH_A = \frac{p_s - p_v}{\rho g} + \frac{c_s^2}{2g} \pm \Delta z_s' \tag{2.7}$$

or

$$NPSH_A = \frac{p_e - p_v}{\rho g} + \frac{c_e^2}{2g} \begin{matrix} +h_z \\ -h_s \end{matrix} - \frac{E_{Rs}}{g} \pm \Delta z_s' \tag{2.8}$$

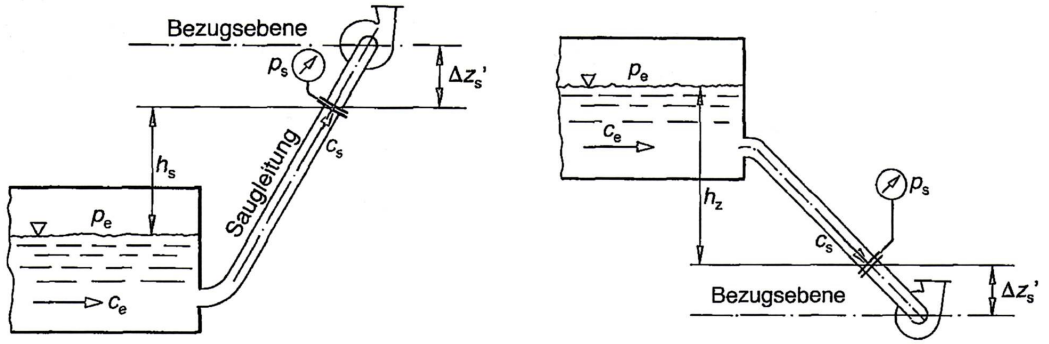

(a) Suction mode (b) Intake mode

Figure 2.8: Reference planes for the NPSH value [2]

The NPSH value can be determined by using the values for the pressure and the velocity of the fluid at the pump inlet (p_s and c_s) or at the tank (p_e and c_e). In the second case the height differences h_s or h_z and the losses in the inlet pipelines E_{Rs} caused by friciton, redirecting and detachment in armatures like pipe bends, valves, diffusers, sliders etc. has to be regarded. The losses are defined by

$$E_{Rs} = (\sum \lambda \frac{l}{d} + \sum \zeta) \frac{c_s^2}{2} \tag{2.9}$$

with the friction coefficient of the pipe λ, the length l and the diameter d of the pipe, the pressure loss coefficient ζ of the armatures and the flow velocity c_s in the pipe.

Two NPSH values have to be distinguished: the NPSH value of the system, which is calculated with the equations above (NPSH available - $\mathrm{NPSH_A}$) and the NPSH value of the pump (NPSH required - $\mathrm{NPSH_R}$), which is specified by the manufacturer in the pump characteristic (see Fig. A.2).

The $\mathrm{NPSH_A}$ value therefore has a static part

$$\frac{p_e - p_v}{\rho g} \begin{matrix} +h_z \\ -h_s \end{matrix} \pm \Delta z_s' = const.$$

and a dynamic part

$$\frac{c_e^2}{2g} - \frac{E_{Rs}}{g} = f(Q)$$

which is depending on the flow rate (see Fig. 2.9). Unless otherwise described the NPSH value is always defined as the $\mathrm{NPSH_A}$ value.

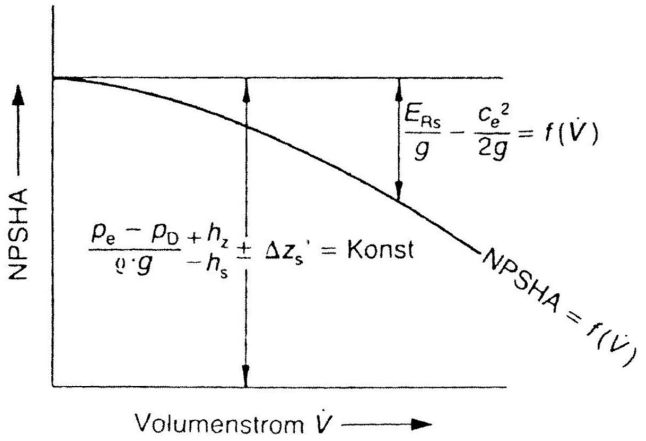

Figure 2.9: Dependence of the $NPSH_A$ value from the flow rate [2]

For the $NPSH_R$ value the criteria for the cavitation intensity has to be specified. Common cavitation criteria are:

- $NPSH_i$: Visual beginning of cavitation (cavitation inception). The first steam bubbles are visible on the blade's suction side.
- $NPSH_x$: Cavitation with x percentage drop of head. The most common criteria is the $NPSH_3$-value (3% drop of head), which is normally published by the pump manufacturers.
- $NPSH_{full}$: Full cavitation - the head of the pump collapses. A two-phase-flow appears in the whole pump.
- Specified drop of efficiency at constant flow
- Specified cavitation erosion on pump components
- Certain level of cavitation-induced noise

To run the pump without cavitation it must be applied that

$$NPSH_A > NPSH_R \tag{2.10}$$

Typical characteristics for the different $NPSH_R$ criteria are shown in Fig. 2.10. The $NPSH_i$ characteristic has a minimum at the flow rate, where the incidence angle is $i_1 = 0$, which is therefore called flow rate at shock-free entry Q_{SF}. At $Q < Q_{SF}$ cavitation bubbles appear at the suction side, which is visible in radial pumps and at $Q > Q_{SF}$ steam bubbles appear at the non-visible pressure side. The $NPSH_x$ values increase sharply at sufficiently high flow levels and this is therefore a limitation for the pump's flow rate.

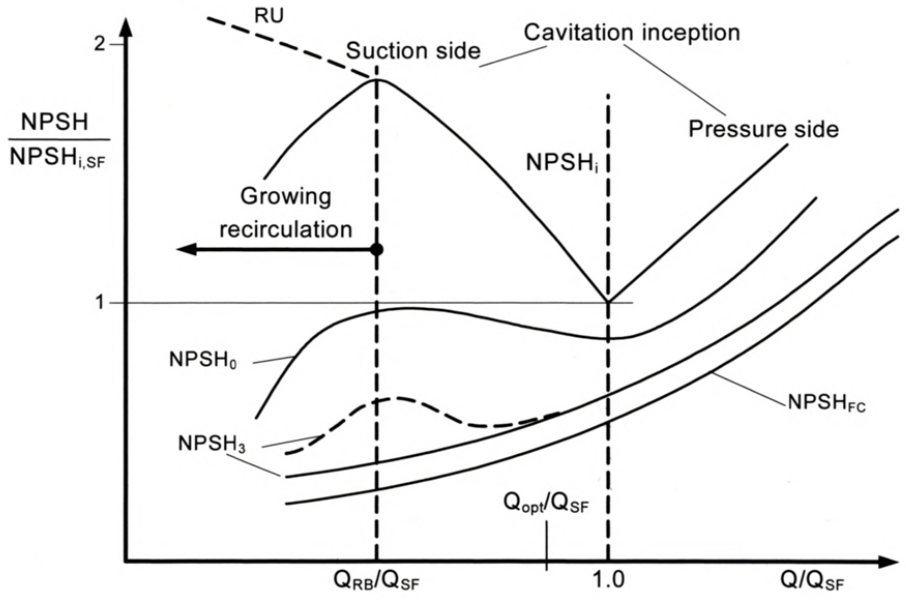

Figure 2.10: Typical NPSH characteristics for centrifugal pumps [1]

2.4 Cavitation Induced Noise and Vibrations

As mentioned in 2.1 the implosion of cavitation bubbles causes pressure waves in the fluid and therefore vibrations and noise in mechanical structures and in the surrounding area. The character of the produced vibrations can be very different depending on the cavitation intensity and on the location where cavitation occurs. Due to the small diameter of the induced steam bubbles the implosion of a few single-bubbles can produce vibrations in the 10 kHz-range up to some MHz if the bubble-radius is in

the μm-range. Unsteady inflow of the runner like turbulences or vortex detachment causes pulsations of the induced bubble area on the runner blade. These fluctuations appear with frequencies beneath 1 or 2 kHz. The sound in the air generated by cavitation is well audible for the human ear because it is in the range of a few hundred Hz and the stochastic impulses are well distinguishable from the machinery noise.

The intensity of the sound pressure in the fluid and so for the vibrations in the mechanical structures is increasing at beginning cavitation. The first visible steam bubbles on the runner appear at lower NPSH values as for the acoustic detectable beginning because very small single-bubbles can occur in the machine before they are visible. With decreasing NPSH values the vibration and sound pressure level (NL) increases to a maximum before it's decreasing to a level, which can be lower than at the starting point (NL_0). In Fig. 2.11 the sound pressure, the erosion rate (E_R) and the potential implosion energy (E_{pot}) are plotted as a function of the cavitation index σ. The reason for the decrease of the vibration intensity is the strong increase of compressible steam bubbles in the fluid at low NPSH values. Therefore the sound pressure in the flow section is damped very strong and cannot reach the casing.

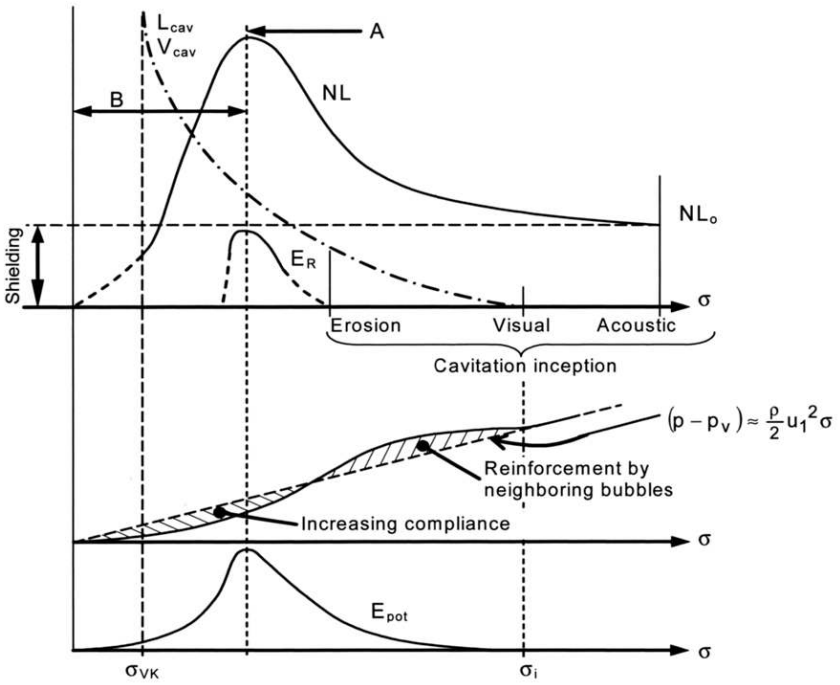

Figure 2.11: Correlation between NPSH value and vibration level [1]

3 Cavitation Monitoring

3.1 Current State of Measurement Systems

The current state of knowledge about the processes of cavitation in hydraulic machinery is well advanced and also diagnose systems for vibro-acoustic cavitation detection produce reliable results. Some of them, like the multidimensional cavitation diagnostics, described in [3], enable a temporally and even spatial (averaged) resolution of the cavitation induced vibrations to locate even their origin. Especially in hydropower or pump storage plants there is no possibility to look inside a turbine or pumpturbine unit during operation, so these systems can give detailed information about the cavitation mechanisms and the cavitating parts of the hydraulic machinery. The disadvantage of such measurement systems is their complexity due to the very high number of various sensors, which have to be mounted on different locations of the unit (see Fig. 3.1).

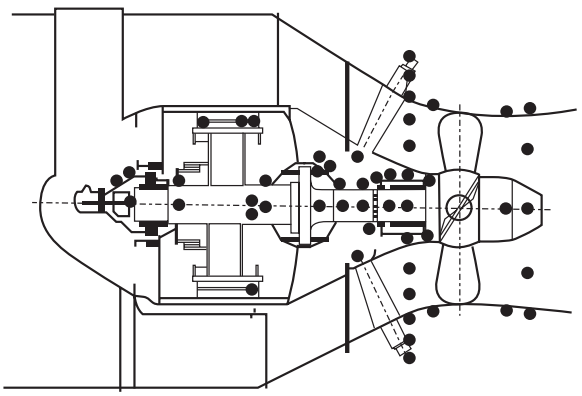

Figure 3.1: Multidimensional cavitation monitoring [5]

To measure the fluid-borne noise induced by cavitation, it is necessary to install special pressure transducers and hydrophones inside the turbine respectively pump-

turbine unit close to the runner blades. But the mounting of those sensors on the inside is not possible in most cases or too expensive for facility operators, because the unit has to be shut down for the installations. In cases of cavitation damages on turbine units, such measurement systems can be furnished during an overhaul and enable an identification of critical turbine parts and an estimation of the cavitation erosion rate [4].

A more simple way for cavitation detection is to measure only the structure-borne noise on the casing of the machine with acceleration transducers. Although a detailed description of cavitation processes inside the machine is hardly to achieve, especially a spatial cavitation resolution, an evaluation of the overall cavitation intensity in the pump or turbine is feasible and sufficient for many applications. Depending on the mounting location of the sensors, an evaluation of critical unit parts is also possible, e.g. if the accelerometers are mounted on the shaft of a turbine's guide vanes.

One disadvantage of measuring the cavitation induced vibrations on the unit's casing is the attenuation factor of the fluid and the casing material itself, so the distance between the cavitation origin and the sensor should be as short as possible, to get reliable results. Another disadvantage is the insufficient determination of the erosive aggressiveness of appearing cavitation because the implosion point of the steam bubbles cannot be detected precisely and so it's hardly possible to determine, if the cavitation has a destructive impact on machinery components, as mentioned in 2.1.

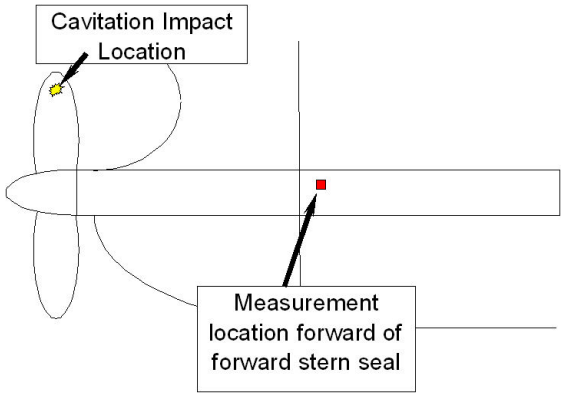

Figure 3.2: Shaft-mounted erosion-detection system [6]

This problem can be remedied by installing a shaft-mounted erosion-detection system, described in [6], where acoustic emission sensors were used, to detect cavitation

damages on ship's propellers and rudders. A schematic description of such a measurement system is shown in Fig. 3.2. The sensors are mounted directly on the rotating shaft of the runner and the vibration signal is transmitted to the data acquisition system by a telemetry set.

The problem of a "significant attenuation caused by the large distance between emission source and sensor"[1] can be avoided by measuring the attenuation "using a Hsu-Nielsen source which generates a signal of known magnitude at a known location"[2]. With this measurement technique the influence of the unknown transfer function through the fluid to the pressure transducers or also through the casing to the accelerometers on the results can be circumvented.

A current feasibility study developed at the *TU Darmstadt* [7] deals with spatially and temporally resolving of cavitation by using thin PVDF (polyvinylidene fluoride, $C_2H_2F_2$) piezoelectric membrane pressure sensors with an eigenfrequency in the GHz range. The advantage of these membranes is their matrix-structure formed by electrode rows and columns. Mounted inside the channel walls a very detailed analysis of cavitation processes is possible, up to resolving collapses of single bubbles, depending on the used measurement electronics and therefore on the sampling rate.

3.2 Erosion Experiments

Another way to determine cavitation, especially locations and components which are affected by steam bubble implosions, is the implementation of erosion experiments. Micro-pitting and erosion damages occur on affected machinery parts, if the cavitation intensity exceeds the strength and resistance of the used material. Due to the long time period until cavitation shows impacts on the material, paint erosion tests or soft metal layers like chopper are used to reduce the time effort during the experiments (see Fig. 3.3). Erosion tests cannot provide on-line cavitation monitoring because the appearing damages have to be investigated after the experiments, although automated pit-count measurement hard- and software have been developed to improve this technique, as described in [9]. But they can help to determine and

[1] Boorsma; Fitzsimmons: Quantification of Cavitation Impacts with Acoustic Emissions Techniques (2009), p. 4

[2] Boorsma; Fitzsimmons: Quantification of Cavitation Impacts with Acoustic Emissions Techniques (2009), p. 2

exceed the lifetime of hydraulic machinery components by applying those experiments on prototypes, especially in combination with the measurement systems mentioned above.

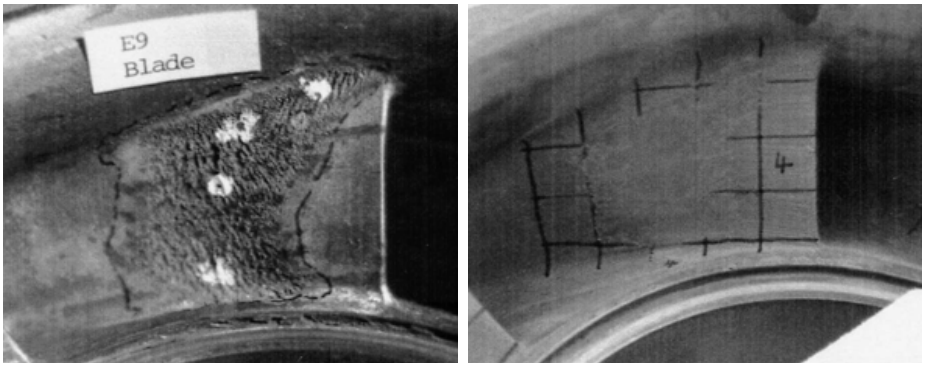

(a) Steel impeller, 9000 min^{-1}/160 h (b) Paint erosion, 3000 min^{-1}/8 h

Figure 3.3: Comparison of erosion tests at a steel impeller and paint erosion [1]

4 Description of the Laboratory Model

4.1 Description of the Test Rig

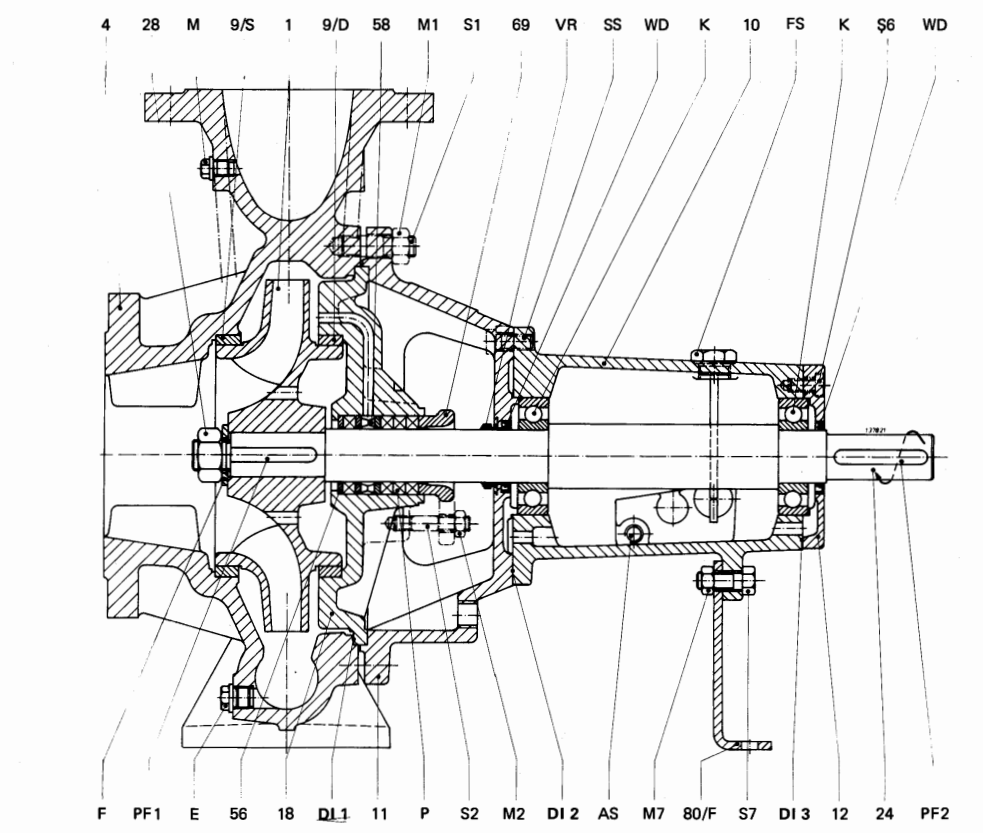

Figure 4.1: Section view of the pump

The measurements for the cavitation detection are implemented on a radial pump with a runner diameter of 296 mm. The section view of the pump is shown in Fig.

4.1 and the data of the pump is listed in Table 4.1. The pump characteristics from the manufacturer are shown in the appendices in Fig. A.2.

Manufacturer	Vogel Pumpen
Type	L 100-315 EN
Construction	Horizontal single stage volute casing pump
Shaft sealing	Standard stuffing box
Lubrication	Oil
Liquids	Water
Temperature of pumped liquid	max. 140 °C
Capacity	150 m^3/h
Head	30 m
Speed	1450 min^{-1}
Power input	max. 22 kW
Impeller diameter	296 mm
Number of runner blades	6
Casing pressure	12 bar
Impeller material	GG
Casing material	GG
Suction branch	DN 125, PN 10 (DIN 2532), horizontal axes
Discharge branch	DN 100, PN 16 (DIN 2533), vertical axes
Shaft bearing type	Ball bearings

Table 4.1: Pump data

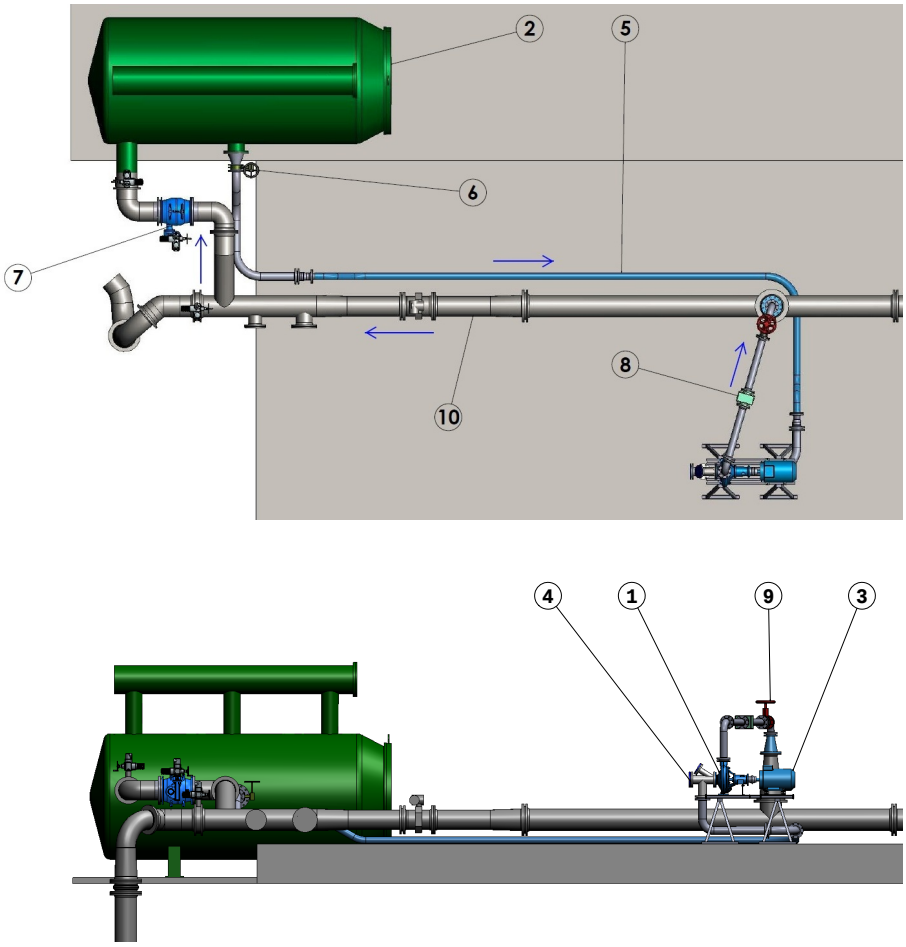

Figure 4.2: Schematic description of the test rig

A schematic description of the test rig is shown in Fig. 4.2: The **radial pump (1)** is running in a circulatory system with a **collection tank (2)** at the end of the pressure pipe respectively at the beginning of the suction pipe. The pump is driven by a 22 kW **electric motor (3)**, which is supplied and controlled by an external frequency converter. The **pump inlet connection (4)** is equipped with two sight glasses, which enables a direct view on the runner blades for a visual cavitation evaluation and documentation, by using a strobe light and a camera. The suction pipe, which consists partially of a flexible **suction tube (5)**, can be closed manually by a **butterfly valve (6)** at the tank connector. The discharge is controlled by an electrical assessable **plunger valve (7)** and is measured with an electromagnetic **flow transducer (8)**. In the pressure pipe there is a **slider (9)** installed, to disconnect

the pump test rig from the **main pipe (10)**.

As mentioned in section 2.3 (Eq. 2.8) the $\mathrm{NPSH_A}$ value is depending on the following parameters: the pressure p_e in combination with an assumed velocity $c_e \sim 0$ m/s at the collection tank (2), the vapour pressure p_v, which is specified by the fluid temperature and velocity, the height difference between the shaft of the pump and the water surface in the collection tank $\begin{smallmatrix} h_z \\ h_s \end{smallmatrix} + \Delta z'_s$ and the losses E_{Rs} at the inlet pipe system (see Eq. 2.9). The height difference and the losses at a given flow are nearly constant, so the only parameter to control the $\mathrm{NPSH_A}$ value and therefore the cavitation intensity in the pump is the pressure p_e at the collection tank (2). The tank is filled between one-half and three-quarter of its height with water, so the tank pressure can be assessed by a valve-system with a vacuum pump, to evacuate the tank to a pressure below the ambient pressure and with an air compressor, to increase the pressure above the ambient pressure. The maximum range for the absolute tank pressure is $0.2 < p_e < 2.0$ bar.

4.2 Description of the Measurement Equipment

A precise description of the whole test rig and measurement equipment is listed in appendix A.1.

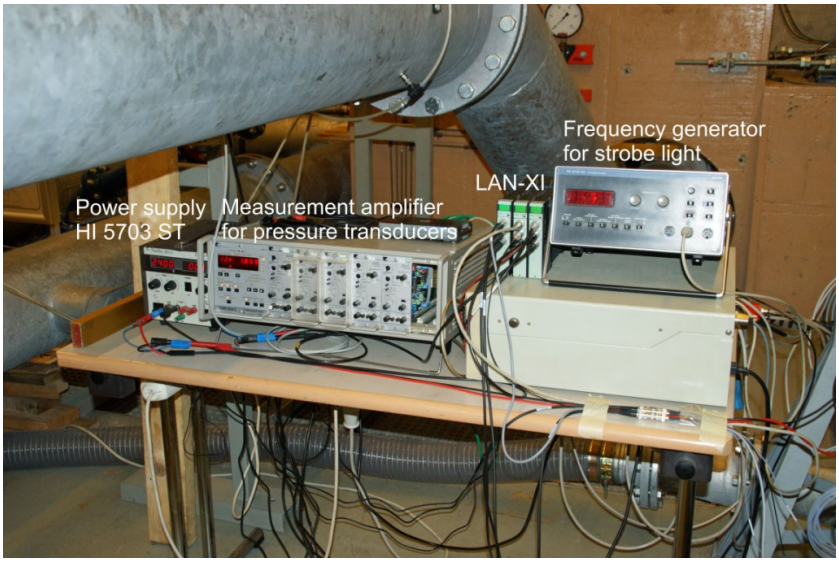

Figure 4.3: Measurement equipment

Data Acquisition Hardware and Software

The equipment for the vibration measurements and for the data acquisition is provided by the company *Brüel & Kjaer Vibro*. The data acquisition hardware consists of three *LAN-XI* frontend modules each with three input channels and a frequency range of 0 to 102.4 kHz (see Fig. 4.3). The data is analysed with the *Brüel & Kjaer PULSE* platform (version 16), especially with the *PULSE LabShop* software for real-time acquisition, the *Time Data Recorder* for signal recording and the *PULSE Reflex Core* for post-processing of the recorded data.

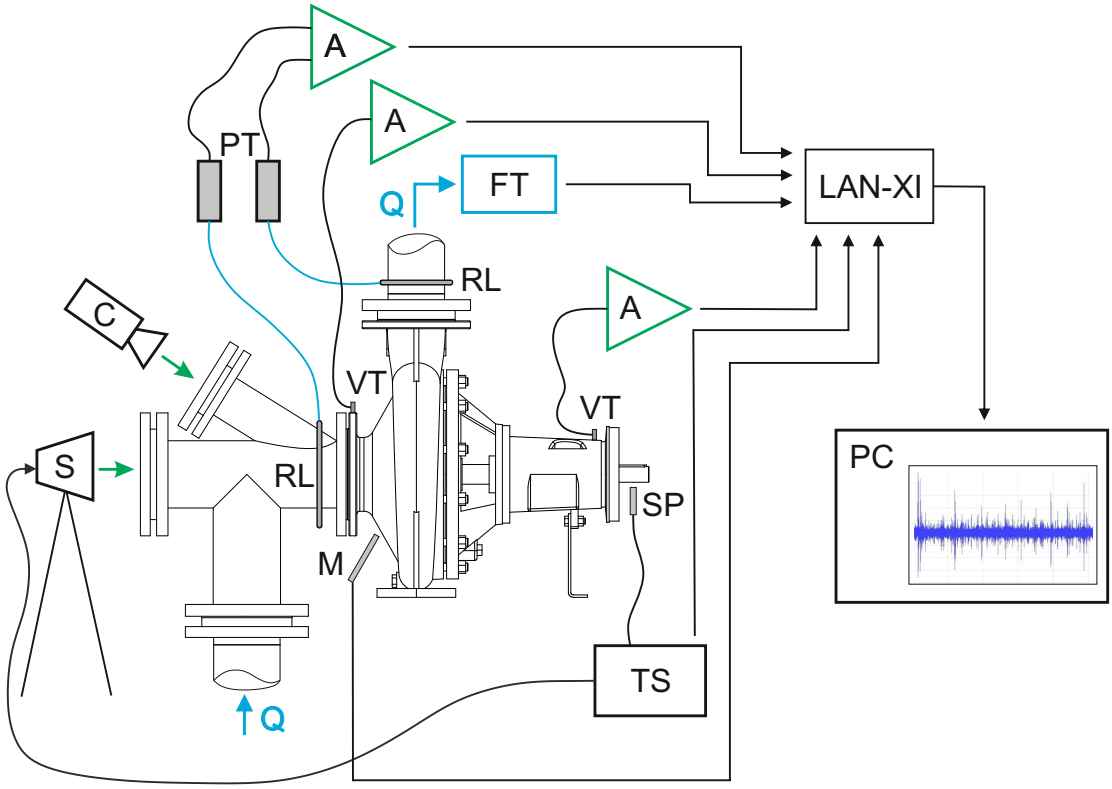

Figure 4.4: Measurement setup schematic

A: Amplifier - external/internal, FT: Flow Transducer, C: Camera, S: Stroboscope, SP: Speed Sensor, TS: Generator for Trigger Signal, PT: Pressure Transducers, VT: Vibration Transducers, M: Microphone Q: Water Flow, RL: Ring Line for Pressure Measurement

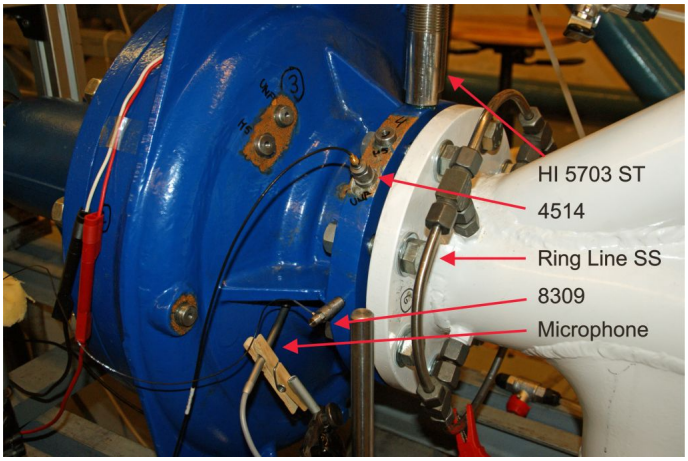

(a) Sensor mountings on the suction side

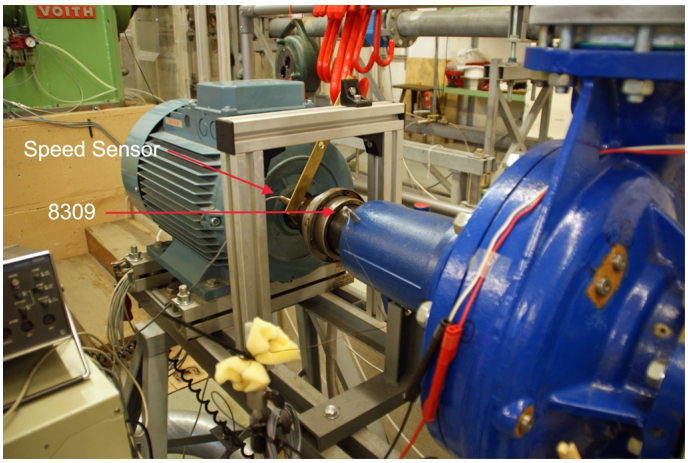

(b) Speed sensor and 8309 on the backside bearing

Figure 4.5: Sensor mountings

Vibration Monitoring

To detect existing cavitation induced vibrations on the casing of the pump, different accelerometers and stress energy transmitters are used with different frequency ranges. For the very high frequencies two 8309 piezoelectric charge shock accelerometers with external charge amplifiers are mounted on the casing. One on the inlet flange of the pump close to the leading edge of the runner blades for a direct detection of cavitation. The other one on the backside bearing to measure the background noise produced by the machine itself and to see, if cavitation induced vibrations can also be detected

through the pump shaft and the ball bearing, as mentioned in section 3.1.

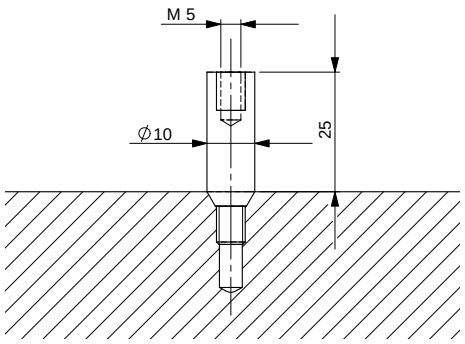

Figure 4.6: Mounting bolt 8309

For an accurate connection to the surface of the casing the 8309 sensors are mounted with mounting bolts (see Fig. 4.6) for a reliable transfer of the vibrations to the accelerometers.

To compare the measurements from the 8309 sensors in the lower frequency range one 4514 piezoelectric shear accelerometer with integrated amplifier is mounted on the inlet flange, which is more sensitive on accelerations than the 8309. To test a more inexpensive measurement system a stress energy transducer HI 5703 ST is also mounted on the inlet flange. The HI 5703 ST uses an external DC power supply.

To pick up the ambient sound noise produced by the machine and perhaps also by cavitation a microphone with implemented pre-amplifier is mounted close to the pump casing at the suction side.

Pressure and Flow Transducers

The pressure on the suction side and on the pressure side is measured with two strain gage technology-based pressure transducers. For a more precise measurement the pressure is picked up through four over the pipe circumference homogeneously distributed drilled holes and a ring line. The pressure transducers are supplied with a two channel measurement amplifier. The setup for the pressure measurements has been calibrated before starting the vibration measurements. The calibration diagram is shown in the appendices in Fig. A.1. The discharge of the pump is measured with an electromagnetic flow transducer installed on the pressure side of the pipe system.

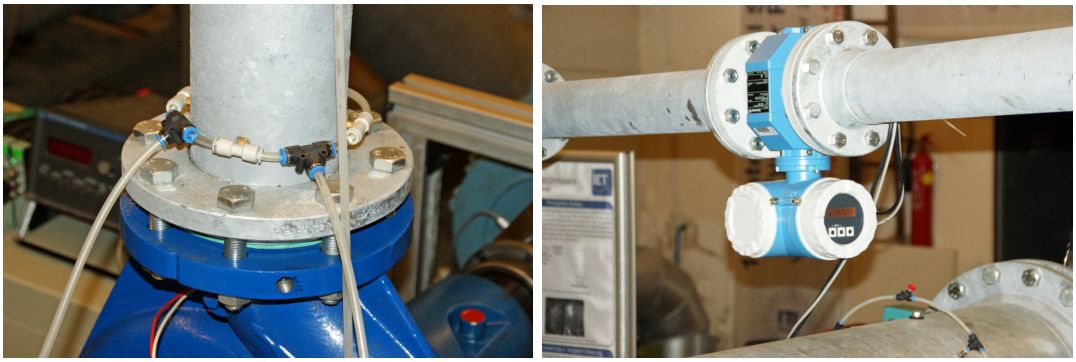

(a) Ring line on the pressure side (b) Flow transducer

Figure 4.7: Pressure and discharge measurement

Speed Sensor and Visual Acquisition

The rotational speed of the pump is picked up with an inductive speed sensor located close to the feather key of the shaft coupling. The stroboscope, used for visual cavitation evaluation, is triggered with the signal from the speed sensor. The triggerable camera shown in Fig. 4.8(a) (*SONY DFW-VL500*) was used to adjust the sensors and the measurements by monitoring the cavitation in the impeller. The disadvantage of this camera is the low resolution of 640 x 480 pixels, so for the documentation itself a *SONY A-350* DSLR camera was used. To get a satisfying picture quality the exposure time was set to 1/20 s, which correlates nearly to the rotational speed of the pump (1450 $\text{min}^{-1} \equiv 24\ \text{s}^{-1}$).

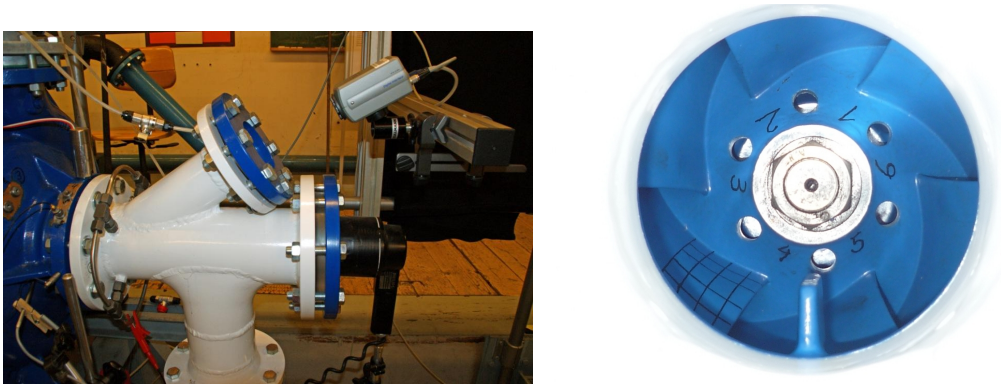

(a) Camera and stroboscope (b) Runner blades

Figure 4.8: Visual cavitation detection

By triggering the stroboscope with the speed of the pump, the camera takes only one picture per flash of the stroboscope, which is equivalent to one picture per revolution. To estimate the size of the cavitation bubbles and the cavity, one of the 6 runner blades was painted with a grid on the surface. The blades where also numbered to distinguish them (see Fig. 4.8(b)).

The vibration sensors, the microphone, the pressure transducers, the flow transducer and the speed sensor are connected by coaxial cables to the LAN-XI modules, which are connected by LAN cables to the computer with the PULSE platform. The measurement setup and the location of the sensors are described in Fig. 4.3 to 4.8.

5 Measurements

5.1 Pump and Cavitation Characteristics

At the beginning of the measurements the pump characteristic and the different NPSH curves are measured to determine the cavitation intensity of the pump in different operation points and to define the measuring points for the cavitation induced vibration detection.

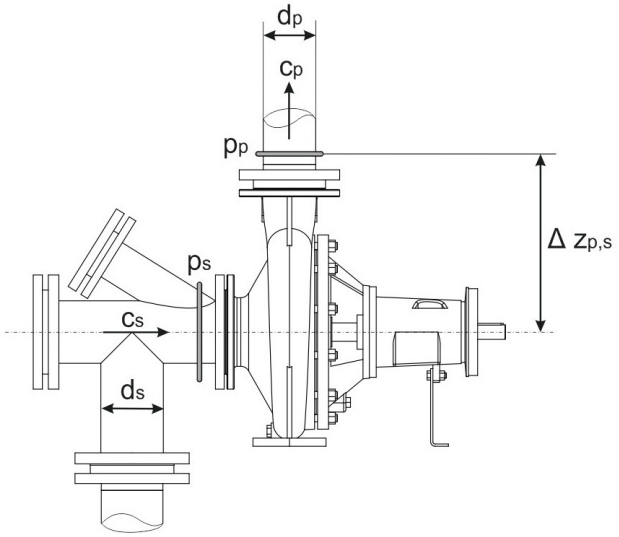

Figure 5.1: Geometry and measurement points for the pump head

The total head of the pump is calculated with

$$H = \frac{p_p - p_s}{\rho g} + \frac{c_p^2 - c_s^2}{2g} + \Delta z_{p,s}[m] \tag{5.1}$$

with the water density $\rho = 998.3 kg/m^3$ at $20°C$ (water properties from Table A.1) and the height difference between the pump shaft and the measuring point for the

pressure on the pressure side $\Delta z_{p,s} = 0.4$ m (see Fig. 5.1). The velocities c_p and c_s are calculated with the measured flow by

$$c_{p,s} = \frac{Q}{A_{p,s}} = \frac{4Q}{\pi d_{p,s}^2} \tag{5.2}$$

with the cross section A and the diameter d of the pressure and the suction pipe $d_s = 100$ mm and $d_p = 125$ mm.

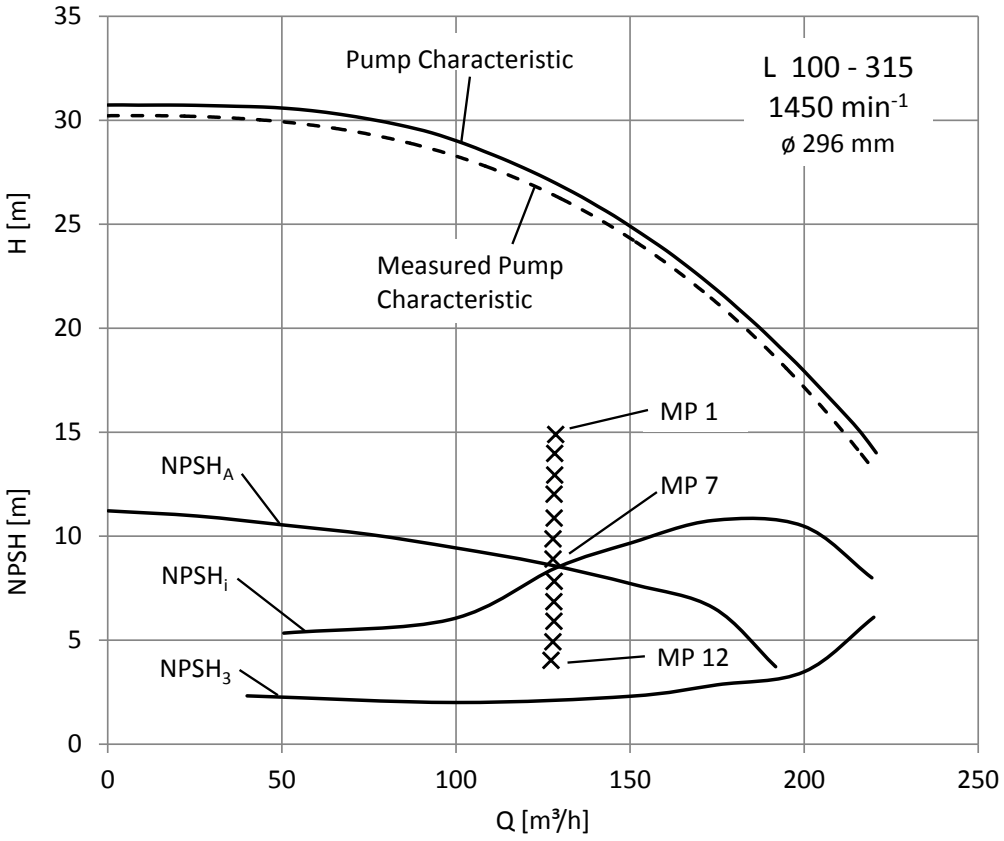

Figure 5.2: Measured pump characteristic and NPSH curves

The measured pump characteristic is shown in Fig. 5.2. Furthermore for comparison the pump characteristic from the manufacturer is also stated. The difference between the two curves is in an acceptable tolerance range.

The NPSH values for the different cavitation characteristics in Fig. 5.2 are calculated with Eq. (2.7), with the vapour pressure of water $p_v = 0.0234$ bar (see Table A.1) and the height difference $\Delta z'_s = 0$ m (the measuring point for the pressure on

the suction side and the pump shaft are on the same reference plane).

The $NPSH_A$ curve was measured at $p_e = 1.1$ bar in the tank, where the exhaust valve was fully opened. For different values of p_e it can be shifted up and down in parallel to the given curve, compared to Eq. 2.8 and Fig. 2.9. The height difference between the water surface in the tank and the pump shaft is $h_z \approx 0.7$ m (the water surface in the tank is above the pump shaft - see Fig. 2.8(b)).

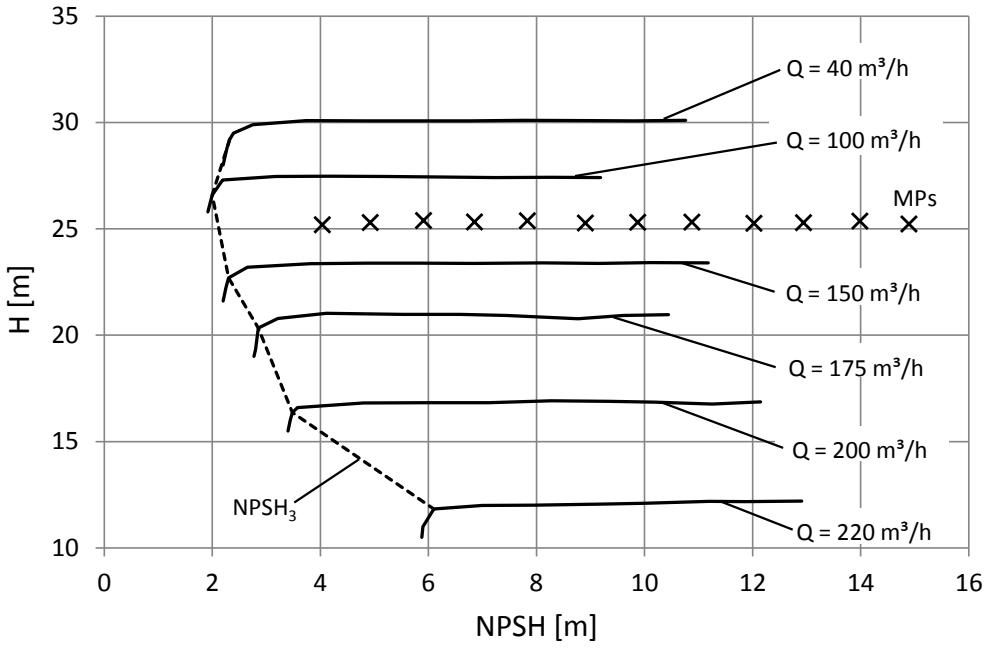

Figure 5.3: Determination of $NPSH_3$

As shown in the pump characteristics from the manufacturer (see Fig. A.2) there are only the $NPSH_R$ curves for the pump types with a runner diameter of 246 mm and 321 mm specified and not for the used type with a runner diameter of 296 mm. But for the measurements it is necessary to know how intense the cavitation in the operational point is. For this reason the $NPSH_3$ curve with a drop of total head of 3 % is determined by measuring the head at constant speed and constant flow while reducing the inlet pressure p_s. The pump head is then plotted as a function of $NPSH_A$. At higher $NPSH_A$ values the suction curve is nearly horizontal because the head is not influenced by cavitation. When the inlet pressure is sufficiently low, more and more steam bubbles appear in the pump and the total head drops down

until it collapses completely (full cavitation - vertical suction curve). To determine the $NPSH_3$ characteristic the "suction curves" are measured at different flow rates. The results are shown in Fig. 5.3. The NPSH values at a 3 % drop of total head for the different flow rates are connected by a dotted line to estimate the values in between. In Fig. 5.2 the values are plotted as a function of the flow, which results to the shown $NPSH_3$ characteristic.

Further on to determine the beginning of cavitation on the runner blades at different flow rates, the $NPSH_i$ values as a function of the flow are illustrated in Fig. 5.2. The values correspond to the first visible appearance of steam bubbles on the blades, when the inlet pressure is reduced at constant flow. As mentioned in section 2.2 and 2.3, cavitation can appear on the suction side and on the pressure side of the blade, depending on the flow rate. In radial pumps only the suction side is directly visible and therefore the flow rate, where the incidence angle is $i_1 < 0$ and where the cavitation appears on the pressure side must be determined. If it is not determined and the cavitation detection is performed in an operational point, where $i_1 < 0$, cavitation induced vibrations would be measured without detecting visible steam bubbles on the suction side, which could lead to misinterpretations.

The incidence angle as a function of the flow rate is calculated by Eq. 2.1 to 2.5. The blade angle β_{1B} and the runner diameters d_1 and d_n are shown in Fig. A.3 and A.4. To verify the simplified calculation of the crossflow section A_1 mentioned in section 2.2, the specific speed n_q of the pump is calculated at the optimum point with the values from Fig. A.2 by

$$n_q = n\frac{\sqrt{Q_{opt}}}{H_{opt}^{\frac{3}{4}}} = 1450\ \text{min}^{-1}\frac{\sqrt{0.04\ \text{m}^3/\text{s}}}{(25.8\ \text{m})^{\frac{3}{4}}} = 25.33\ \text{min}^{-1} \tag{5.3}$$

which is in the low range for radial pumps.

With the values $\beta_{1B} = 16\,^\circ$, $d_1 = 160\,\text{mm}$, $d_n = 54\,\text{mm}$, the rotational speed $n = 1450\ \text{min}^{-1}$, the assumed leakage factor $\eta_l = 0.95$ to calculate the flow rate Q_{Im} through the impeller and the angle $\alpha = 90\,^\circ$ for an axial inflow, the incidence angle is with

$$A_1 = \frac{\pi(d_1^2 - d_n^2)}{4} = 0.018\ \text{m}^2 \tag{5.4}$$

and

$$u_1 = \frac{\pi d_1 n}{60} = 12.15 \text{ m/s} \tag{5.5}$$

$$i_1 = \beta_{1B} - \arctan \frac{Q_{Im}}{A_1 u_1} = \beta_{1B} - \arctan \frac{Q}{A_1 u_1 \eta_l} = f(Q) \tag{5.6}$$

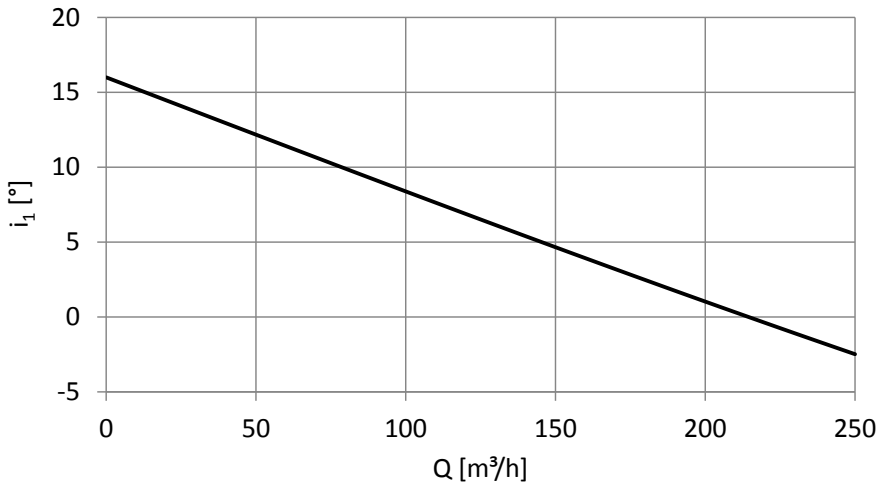

Figure 5.4: Incidence angle as a function of the flow rate

Fig. 5.4 shows the incidence angle i_1 as a function of the flow rate. The value of the flow rate, where $i_1 = 0$ is approximately at $Q = 220$ m^3/h, which is also the upper limit of the pump's flow rate and so, if cavitation occurs, steam bubbles will always occur on the blade's suction side. Compared to Fig. 5.2, where the $NPSH_i$ characteristic drops down again from its maximum at about 180 m^3/h, this means, that the cavitation bubbles appear increasingly on the blade's pressure side at higher flow rates, but there are still steam bubbles visible on the suction side.

5.2 Description of the Measurement Process

The operating point for the vibration measurements was chosen at a flow rate of $Q \approx 130$ m^3/h and a corresponding total head of $H \approx 26$ m. At this point the visible cavitation in the pump is beginning at ambient pressure in the tank ($NPSH_A$ and $NPSH_i$ curves are crossing in Fig. 5.2). So, for a decrease of the cavitation intensity,

p_e has to be raised with the air compressor and for an increase of cavitation, p_e has to be lowered by evacuating the tank.

The measurements were processed at constant speed $n = 1450\,\mathrm{min}^{-1}$ and at an approximately constant flow rate (especially at lower $\mathrm{NPSH_A}$ values the total head and also the flow rate is decreasing because of the accumulation of steam bubbles). The only altering parameter is the tank pressure and therefore the $\mathrm{NPSH_A}$ value. For a precise determination of the cavitation induced vibrations, 12 measurement points (MPs) were recorded. For each measurement point, the pressure in the tank p_e was adjusted and the related parameters like the flow rate, the pressure on the suction and the pressure side and the exact rotational speed were logged. The total head, the $\mathrm{NPSH_A}$ value and the flow velocities were calculated by the known equations. The signals from the vibration sensors and the microphone were recorded with the *Time Data Recorder* and the pictures for the visual evaluation were taken with the camera for each MP. The time signals, with a recorded length of 1 s, which corresponds to approximately 24 revolutions, were post-processed with the *PULSE Reflex Core*. The parameters for the measuring points are shown in Table 5.1 and plotted in Fig. 5.2 from top down and in Fig. 5.3 from right to left.

MP	$\mathbf{p_e}$	**Q**	**H**	$\mathbf{NPSH_A}$	$\mathbf{p_s}$	$\mathbf{p_p}$	$\mathbf{c_s}$	$\mathbf{c_p}$
	bar	$\mathrm{m^3/h}$	m	m	bar	bar	m/s	m/s
1	1.70	128.65	25.23	14.89	1.38	3.87	4.55	2.91
2	1.60	128.36	25.36	13.98	1.29	3.80	4.54	2.91
3	1.50	128.36	25.29	12.94	1.19	3.69	4.54	2.91
4	1.40	128.19	25.26	12.02	1.10	3.59	4.53	2.90
5	1.30	128.21	25.31	10.87	0.99	3.49	4.53	2.90
6	1.20	127.87	25.31	9.87	0.89	3.39	4.52	2.89
7	1.10	127.88	25.27	8.90	0.79	3.29	4.52	2.89
8	1.00	128.22	25.38	7.83	0.69	3.19	4.54	2.90
9	0.90	128.12	25.32	6.85	0.59	3.09	4.53	2.90
10	0.80	128.14	25.39	5.91	0.50	3.01	4.53	2.90
11	0.70	127.84	25.29	4.92	0.40	2.90	4.52	2.89
12	0.60	127.30	25.19	4.03	0.32	2.80	4.50	2.88

Table 5.1: Parameters for the measuring points

It is noticeable, that the $NPSH_A$ value of the last measurement point (MP 12) is higher than the $NPSH_3$ value at this flow rate. This relies on the circumstance, that a visual evaluation of the cavity is not possible due to the high release of steam bubbles at very low NPSH values (the steam bubbles obscure the view on the runner through the sight glass at the pump's inlet - see Fig. 5.5 at MP 12). But this has no impairment on the measurements itself as we will see in section 5.3, because the cavitation is intense enough at this measurement point, to get reliable results and therefore it's not necessary to go deeper into cavitation.

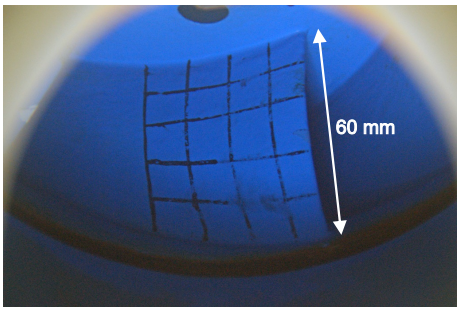

(a) MP 1

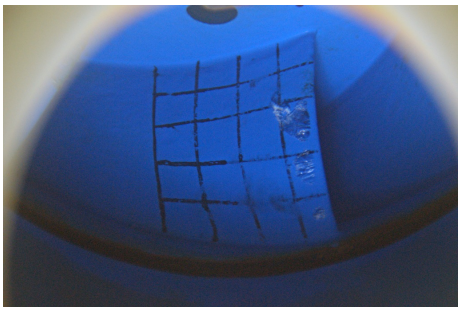

(b) MP 7

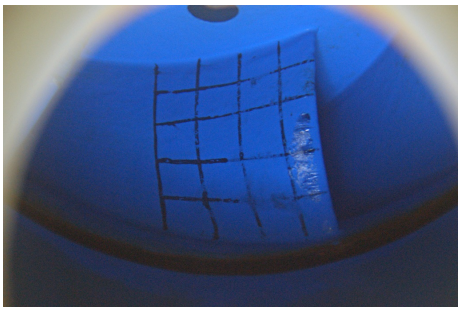

(c) MP 7

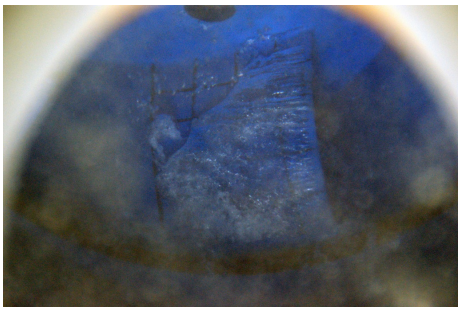

(d) MP 12

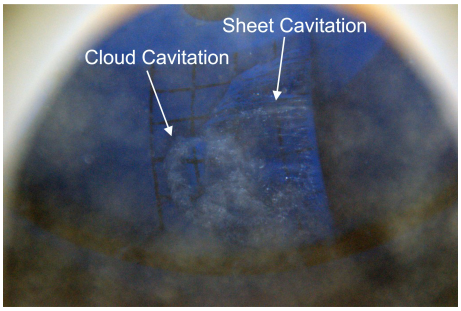

(e) MP 12

Figure 5.5: Visual cavitation detection for the different MPs

5.3 Measurement Results

The results of the vibration measurements are shown and explained by three chosen points of the 12 MPs: The first point is MP 1 with a sufficiently high NPSH value, so there is no cavitation in the pump. The second one is MP 7 with beginning visual cavitation and the last one is MP 12 in the strong cavitation area. The results are sectioned in the analysis in the time history domain (histograms, RMS values) and in the frequency domain (FFT, envelope detection).

The intensity of the cavitation is illustrated with the pictures taken from the runner blade at the three measuring points (see Fig. 5.5). At MP 1 the NPSH value is sufficiently high so that no cavity occurs in the pump. The two pictures at MP 7 show the appearing cavity at the cavitation inception $\mathrm{NPSH_i}$. The steam bubbles occur a few millimetres behind the leading edge, where the static pressure is at its minimum, but they are not distributed along the whole length of the blade's leading edge. The unsteady behaviour of cavitation is also obvious: In the first picture at MP 7 three smaller cavitation areas appear, whereas in the other image the cavity is limited to one bigger zone. In some other pictures taken with the camera, hardly any steam bubbles are visible. At MP 12 the cavity is fully developed and embraces nearly the complete grid marked on the blade. It is noticeable, that two arising cavitation phenomena can be distinguished: Sheet cavitation and cloud cavitation. Experiments in a convergent-divergent nozzle test rig [8] have shown, that the transition from one to the other condition depends on the cavitation number σ respectively on the NPSH value and the dimensionless Reynolds number

$$Re = \frac{\bar{c}h}{\nu} \tag{5.7}$$

with the mean flow velocity at the entry $\bar{c}$, the channel height h and the kinematic viscosity of the fluid ν. Sheet cavitation appears at the point with the lowest static pressure and its dimension growth with a decreasing NPSH value and an increasing Reynolds number. The impeller geometry is predefined from the manufacturer and the kinematic viscosity is depending on the fluid and the temperature, which can be assumed nearly constant for the most applications. So the Reynolds number is primarily changing with the flow velocity and therefore with the flow rate in the pump.

If the sheet is big enough, a part of it is shed as a separated cloud and carried along with the flow. The sheet consists mainly of steam bubbles, which are fused together and has therefore a coherent surface. The cloud is separated from the sheet by a vortex called "reentrant jet", which undermines the sheet as a backflow in the direction of the leading edge (see Fig. 5.6). The cloud consists in contrast to the sheet of many single steam bubbles, which are induced by the shear forces of the reentrant jet.

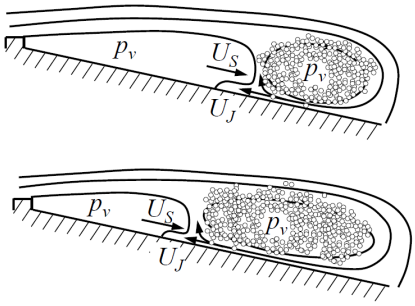

Figure 5.6: Cloud separation induced by the reentrant jet [8]

Cloud cavitation is observed to cause higher damages than sheet cavitation:

> "In the cloud regime, the sheet grows to its maximum length as the cloud moves downstream and collapses. During the sheet growth the kinetic energy of the flow is transferred to the sheet and stored there until the cloud is separated. This energy concentrating process makes cloud cavitation to the most harm full cavitation regime."[1]

In [7] the appearing frequencies of the cloud collapses in the low frequency domain could be verified by a visible detection of the collapsing process with high-speed cameras. Further the determination of the fluctuation frequency on individual profiles, like the nozzle used in the studies in [7] and [8], can be observed by the Strouhal number

$$St = \frac{fl}{c} \tag{5.8}$$

where f denotes the collapsing frequency, l is a characteristic length like the dimension of the obstacle or the cavity length and c is the characteristic velocity (e.g. the inflow

[1] Keil; Pelz; Buttenbender: On the Transition from Sheet to Cloud Cavitation (2012), p.1

velocity). In contrast to special profiles the fluctuation in pumps or turbines is not constant and varies at the different impeller blades, which leads to a broadband signal in the frequency range. This circumstance impedes the detection of cloud cavitation in hydraulic machines.

5.3.1 Cavitation Detection in the Time Domain

In Fig. 5.7 to 5.9 the time history signals for the different vibration sensors and the microphone together with the correlated signal of the speed sensor at the three measuring points are shown. At MP 1 compared to the 4514 and 8309 accelerometers mounted on the pump casing, the 8309 transducer on the backside bearing perceives higher amplitudes due to the vibrations of the ball bearing element. The time history diagrams of the other accelerometers just show the background noise of the machinery without any remarkable peaks. At the other two measuring points with beginning cavitation and strong cavitation the 8309 sensor on the pump and the 4514 sensor perceive very high amplitudes occurring irregularly, which can be therefore correlated to the stochastic implosions of the cavitation induced steam bubbles.

The vibration signals of the 8309 transducer mounted on the backside bearing hardly change with decreasing NPSH values, except for two bigger peaks at MP 12. A correlation between the time history of the 8309 sensor on the bearing and the cavitation intensity is not possible in that way. One reason could be an excessive attenuation between the origin of cavitation and the measuring point so that the cavitation induced noise is covered by the higher peaks of the bearing, or the distance between the implosions of the steam bubbles and the runner surface is too big to cause any vibration excitations. The latter would also imply, that the appearing cavitation has no harmful impact on the runner surface.

The time signals of the stress energy transducer HI 5703 ST and the microphone show no noticeable differences between the three measuring points and allow therefore no conclusion to the cavitation intensity.

Resulting from the consideration of the time history diagrams only the measurements with the 8309 and 4514 accelerometers mounted on the pump casing show a direct connection to the arising cavitation in the pump at the different measuring points.

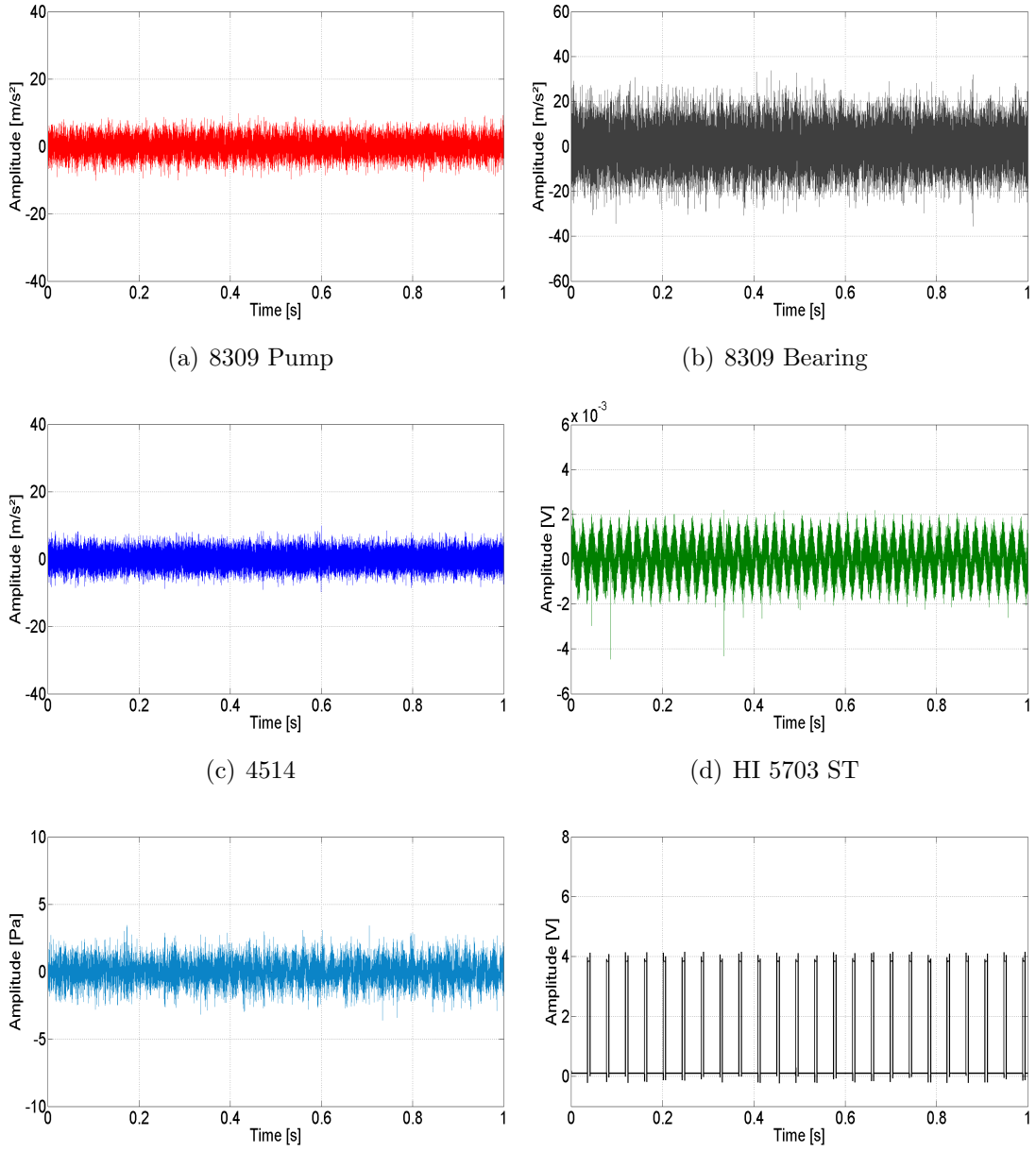

(a) 8309 Pump

(b) 8309 Bearing

(c) 4514

(d) HI 5703 ST

(e) Microphone

(f) Speed sensor

Figure 5.7: Time signals at MP 1

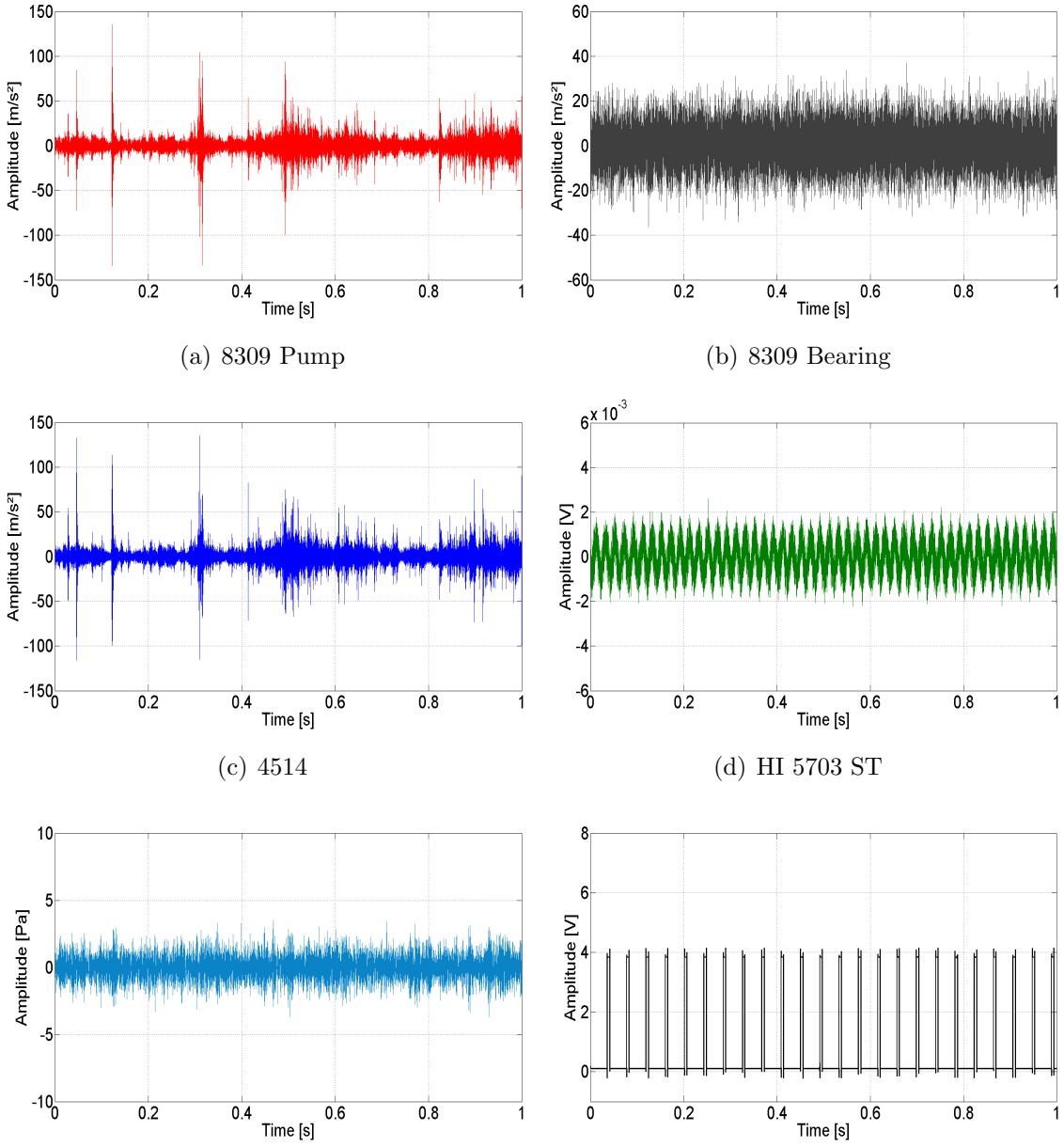

(a) 8309 Pump

(b) 8309 Bearing

(c) 4514

(d) HI 5703 ST

(e) Microphone

(f) Speed sensor

Figure 5.8: Time signals at MP 7

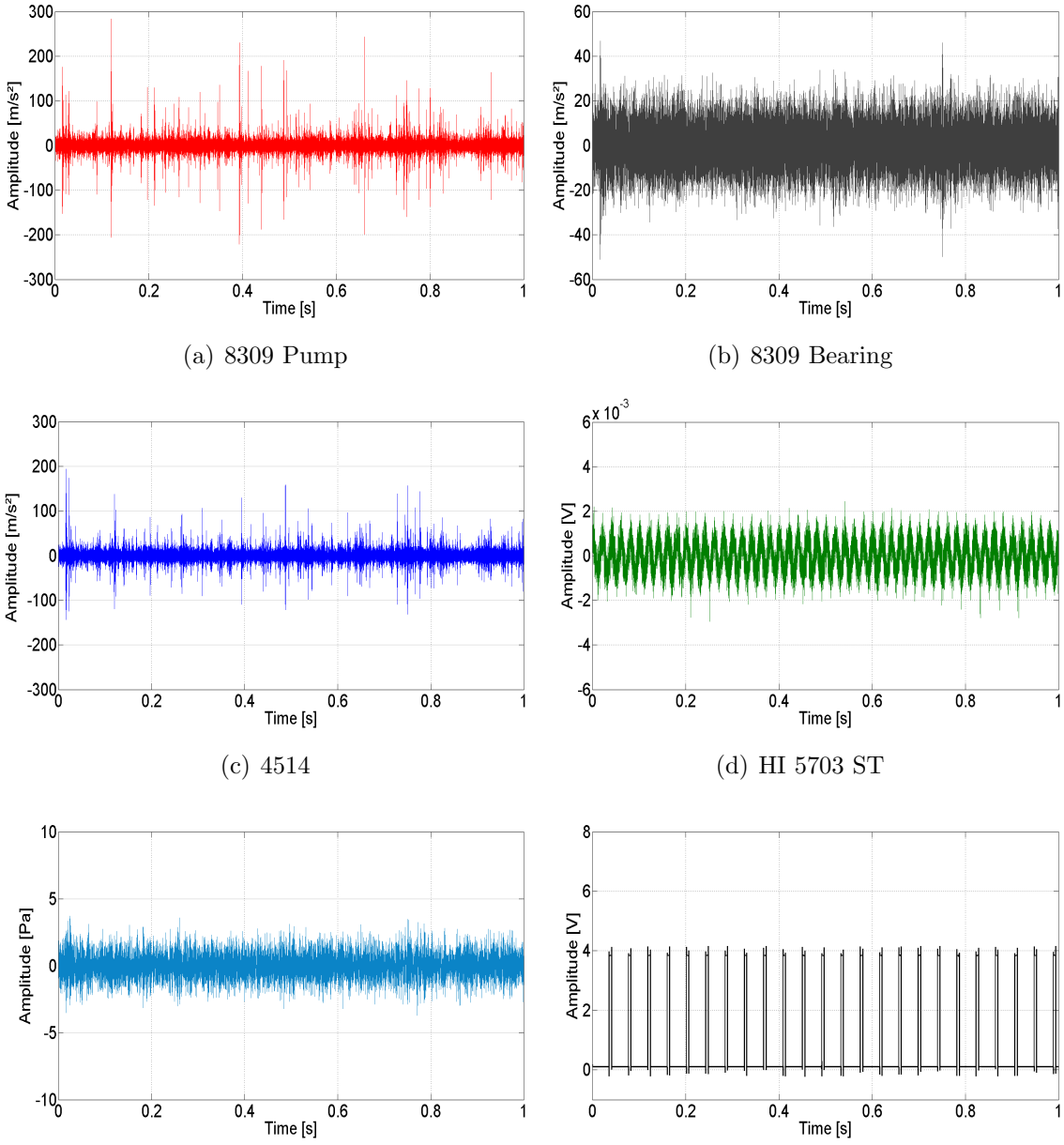

(a) 8309 Pump

(b) 8309 Bearing

(c) 4514

(d) HI 5703 ST

(e) Microphone

(f) Speed sensor

Figure 5.9: Time signals at MP 12

For a statistical analysis of the recorded time signals the amplitude rates for the two vibration sensors at the different MPs are shown in histograms divided into different acceleration classes (see Fig. 5.10). They substantiate the results from the time history diagrams, that the acceleration amplitudes are getting bigger and more frequent with decreasing NPSH values.

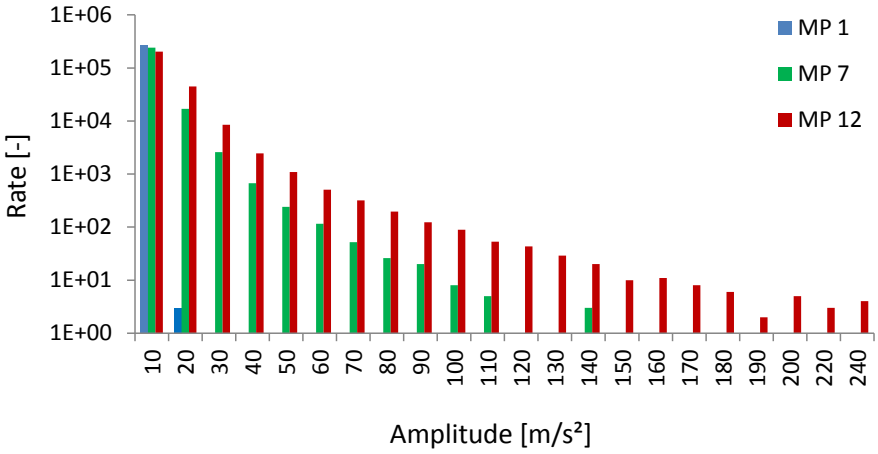

(a) 8309 Pump

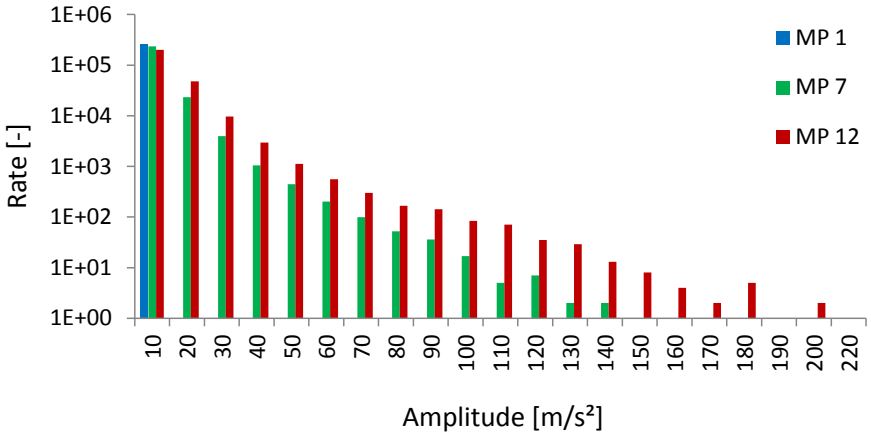

(b) 4514

Figure 5.10: Histograms of the accelerometers

Another method for cavitation detection in the time domain is to calculate the root mean square value (RMS) of the time signal, which represents the energy of the

signal. In Fig. 5.11 the RMS values of all measuring points are plotted as a function of the NPSH value. While the values of the 8309 sensor on the bearing remain fairly constant at a level of about 8 m/s^2 and are visibly not affected by cavitation, the RMS values of the two accelerometers on the pump casing are increasing dramatically with a drop of the NPSH value. The beginning of cavitation can be estimated at an NPSH value of about 11 m (MP 5), which is higher than the visible cavitation beginning at $NPSH_i$, because the first appearing and imploding steam bubbles generate pressure gradients and vibrations in the pump before they are visible for the human eye or visual detection systems. Figure 5.11 shows, that the degree of cavitation can be correlated adequate to the root mean square value of the acceleration signals.

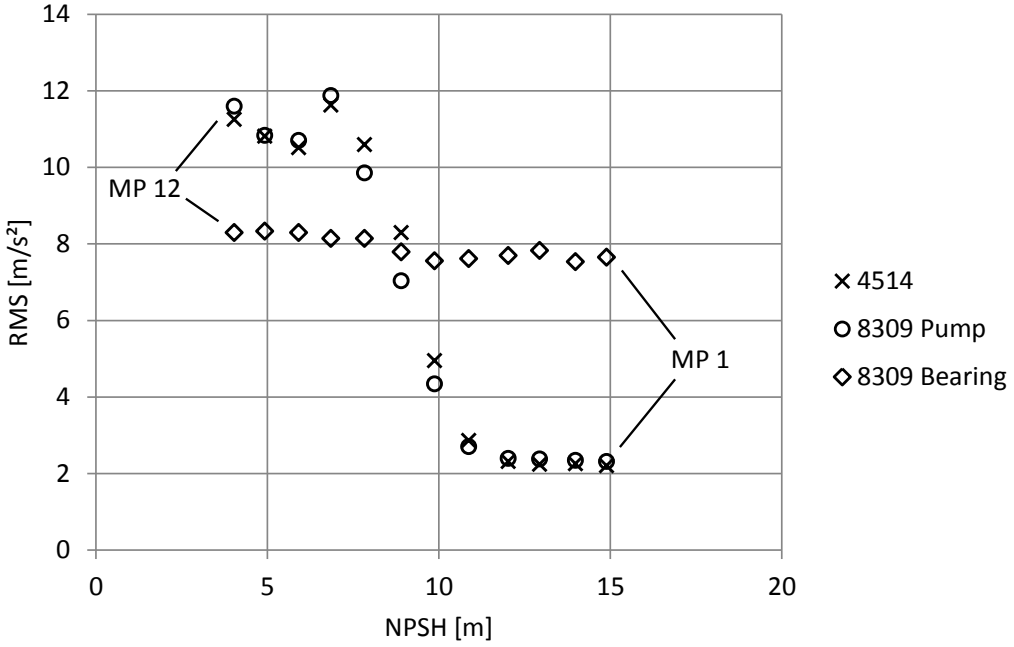

Figure 5.11: RMS values of the accelerometers

5.3.2 Cavitation Detection in the Frequency Domain

As mentioned in section 2.4 cavitation induces vibrations with a broad band structure in the frequency domain. To detect the appearing frequencies in the time signals of the used accelerometers, frequency spectra of the recorded data are created with the *Pulse Reflex Core* by using the fast Fourier transform (FFT). The results for the FFT

analysis are shown in Fig. 5.12 and 5.13 for the full frequency range up to 100 kHz and in the lower frequency range between 0 and 400 Hz.

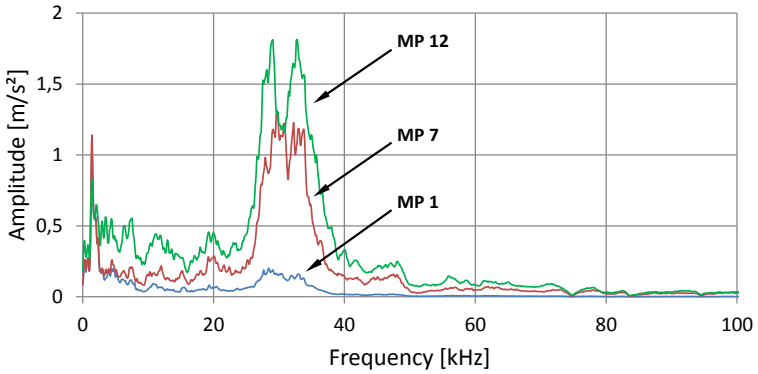

(a) 4514

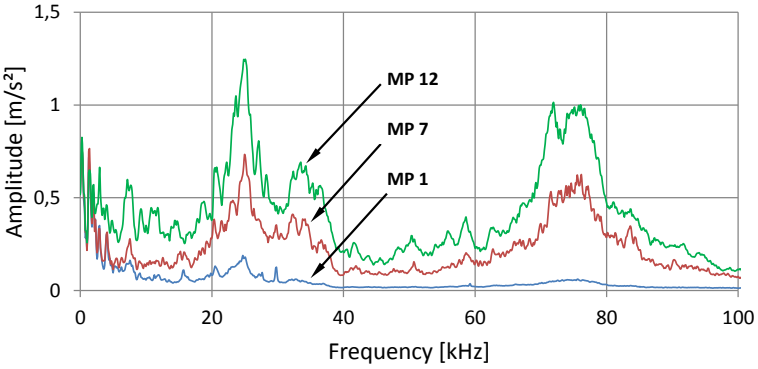

(b) 8309 Pump

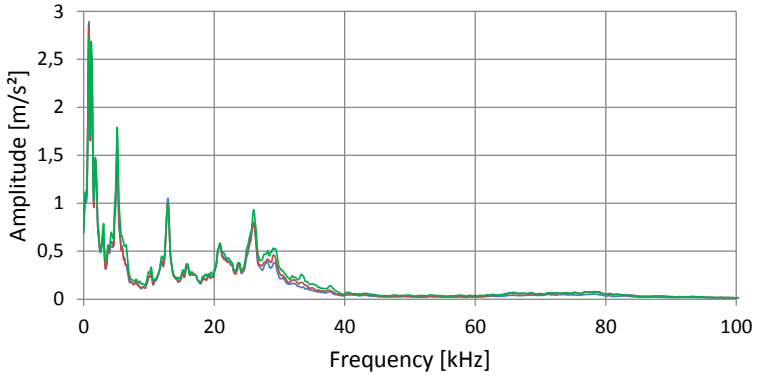

(c) 8309 Bearing

Figure 5.12: FFT diagrams of the accelerometers in the full frequency range

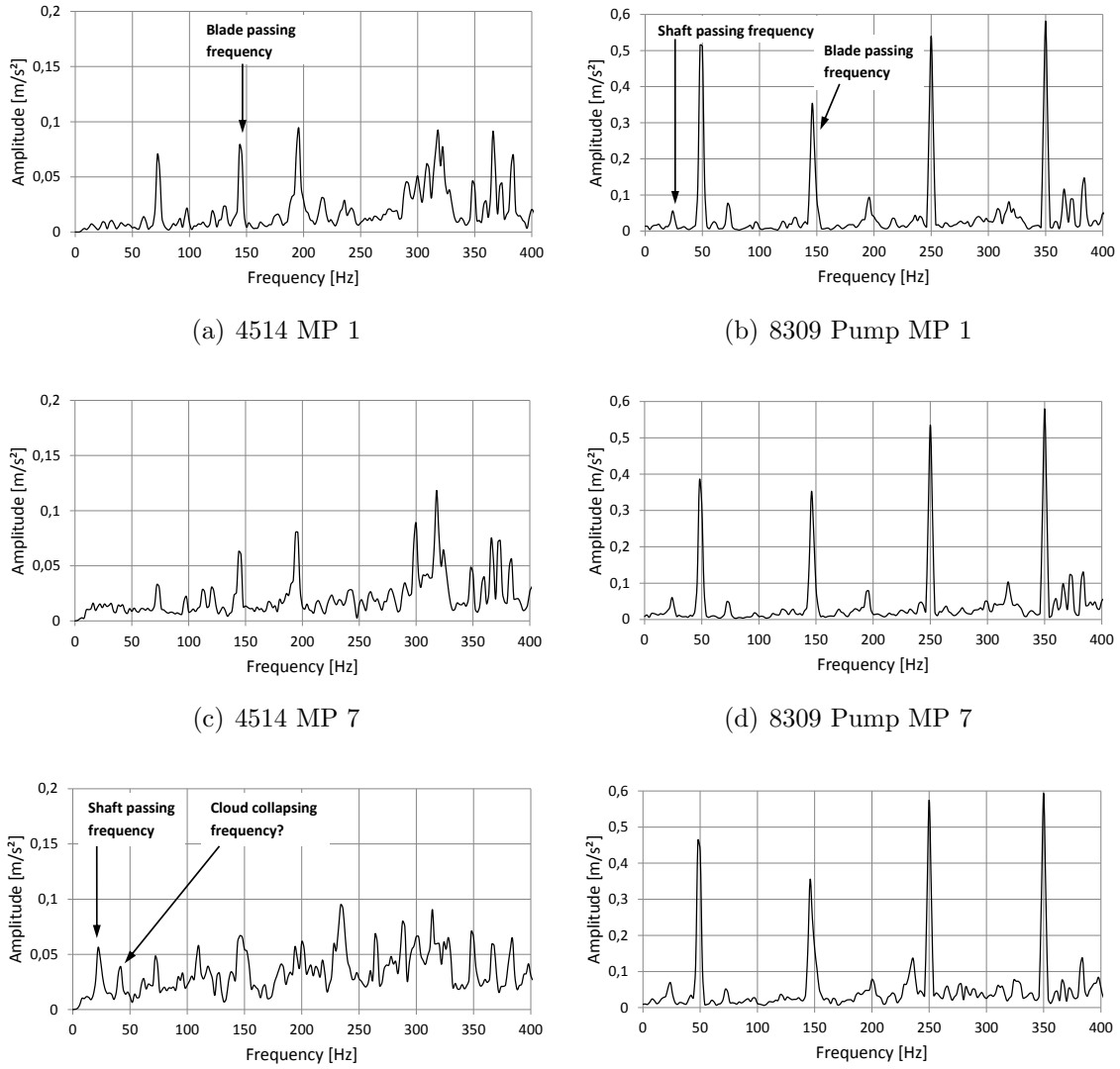

(a) 4514 MP 1

(b) 8309 Pump MP 1

(c) 4514 MP 7

(d) 8309 Pump MP 7

(e) 4514 MP 12

(f) 8309 Pump MP 12

Figure 5.13: FFT diagrams of the accelerometers in the low frequency range

The impacts on the spectra in Fig. 5.12 induced by arising steam bubble implosions show influences in the whole frequency range as estimated. But the biggest differences between the MPs for the accelerometers on the pump casing appear in the higher frequency ranges between 25 kHz to 40 kHz for the 4514 sensor and between 20 to 40 kHz and 60 to 90 kHz for the 8309 sensor. The distinctions in the lower frequency range below 20 kHz are not so remarkable, so the cavitation induced vibrations are very good distinguishable from the machinery sound, which occurs primary in the

low frequency range. The different spectra of the 8309 sensor on the bearing show no noticeable distinctions in any frequency range, which confirms the results from the time domain.

In the FFT diagrams the difference between the measurement ranges of the two accelerometers is clearly recognizable: The drop in the frequency signal of the 4514 transducer at approximately 50 kHz marks the upper limit for its frequency range and the signal above is only noise. The 8309 sensor is able to detect frequencies up to 100 kHz and reveals therefore cavitation induced vibrations also in the higher range. This approves the fact, that it is very important to use appropriate sensors for a cavitation detection system.

In the diagrams for the 4514 accelerometer in the low frequency range (see Fig. 5.13 a, c, e) the blade passing frequency

$$f_b = \frac{nb}{60} = 145 \text{ Hz} \tag{5.9}$$

of the runner is visible. The diagram for the measuring point 12 (see Fig. 5.13(e)) additionally reveals the shaft passing frequency

$$f_s = \frac{n}{60} = 24.17 \text{ Hz} \tag{5.10}$$

which could be ascribed to the strong cavitation in that point. In Eq. 5.9 and 5.10 $n = 1450\,\text{min}^{-1}$ denotes the rotational speed and b = 6 denotes the number of the runner blades. Conspicuous in Fig. 5.13(e) is an appearing amplitude peak at approximately 42 Hz, which could be induced by the beginning cloud cavitation described above. A verification of this assumption was unfortunately not possible due to the lack of a high-speed camera.

The FFT diagrams for the 8309 accelerometer in Fig. 5.13 (b, d, f) also show the blade and the shaft passing frequency at 145 Hz and 24 Hz, but there are also electromagnetic disturbances occurring at the grid frequency of 50 Hz and it's harmonics at 150 Hz, 250 Hz and 350 Hz caused by the frequency converter. Since the sensitivity of the piezoelectric sensors for electromagnetic influences, different measures like shielding of the power cable between the frequency converter and the electric motor or grounding of the data acquisition modules have been taken, to reduce the disturbances to an acceptable minimum. But the influences are still visible in the very low frequency range of the 8309 sensor. In the higher frequency domain the in-

terferences could be removed nearly entirely (see Fig. 5.14). The disturbance signals in the two diagrams were recorded when the frequency converter was started but the electric motor was not running, to expose only the influence of the electromagnetic disturbances.

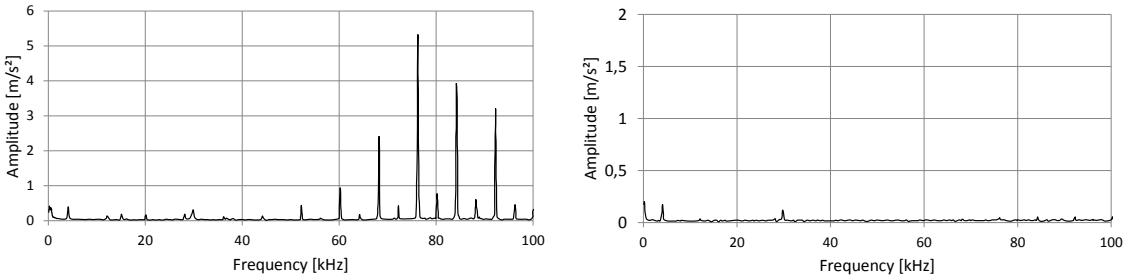

(a) Disturbances previously

(b) Disturbances afterwards

Figure 5.14: Electromagnetic disturbances for the 8309 accelerometer

In Fig. 5.13(f)) the amplitude peak at 42 Hz, ascribed to the cloud cavity, is also visible, even though it's partially covered by the electromagnetic disturbances at 50 Hz.

Comparing the FFT diagrams in the low frequency range for both accelerometers, it's obvious, that the 4514 sensor is hardly influenced by the occurring electromagnetic disturbances. The blade passing frequency is visible at all MPs for both sensors, but the shaft passing frequency occurs only at MP 12 for the 4514 accelerometer. However the diagrams in the low frequency range reveal no dramatic changes due to an increasing cavitation, except another appearing peak at approximately 235 Hz at MP 12.

Another cavitation detection method described in [10] is the demodulation of high pass or band pass filtered cavitation signals. The background of this measurement technique is that when cavitation appears in a rotating machine, the periodicity of it's components modulates the vibration signals induced by the steam bubble implosions in relation to a fixed accelerometer. Since not only the cavitation generated noise affects the modulation, but also machinery noise, the raw signal has to be filtered to detect discrete frequencies like the blade passing and the shaft passing frequencies. Several demodulation techniques exist like half- or full wave rectification or the Hilbert transforms. The latter was used to perform the demodulation spectra shown in Fig.

5.15 at different high pass respectively band pass filtered frequencies.

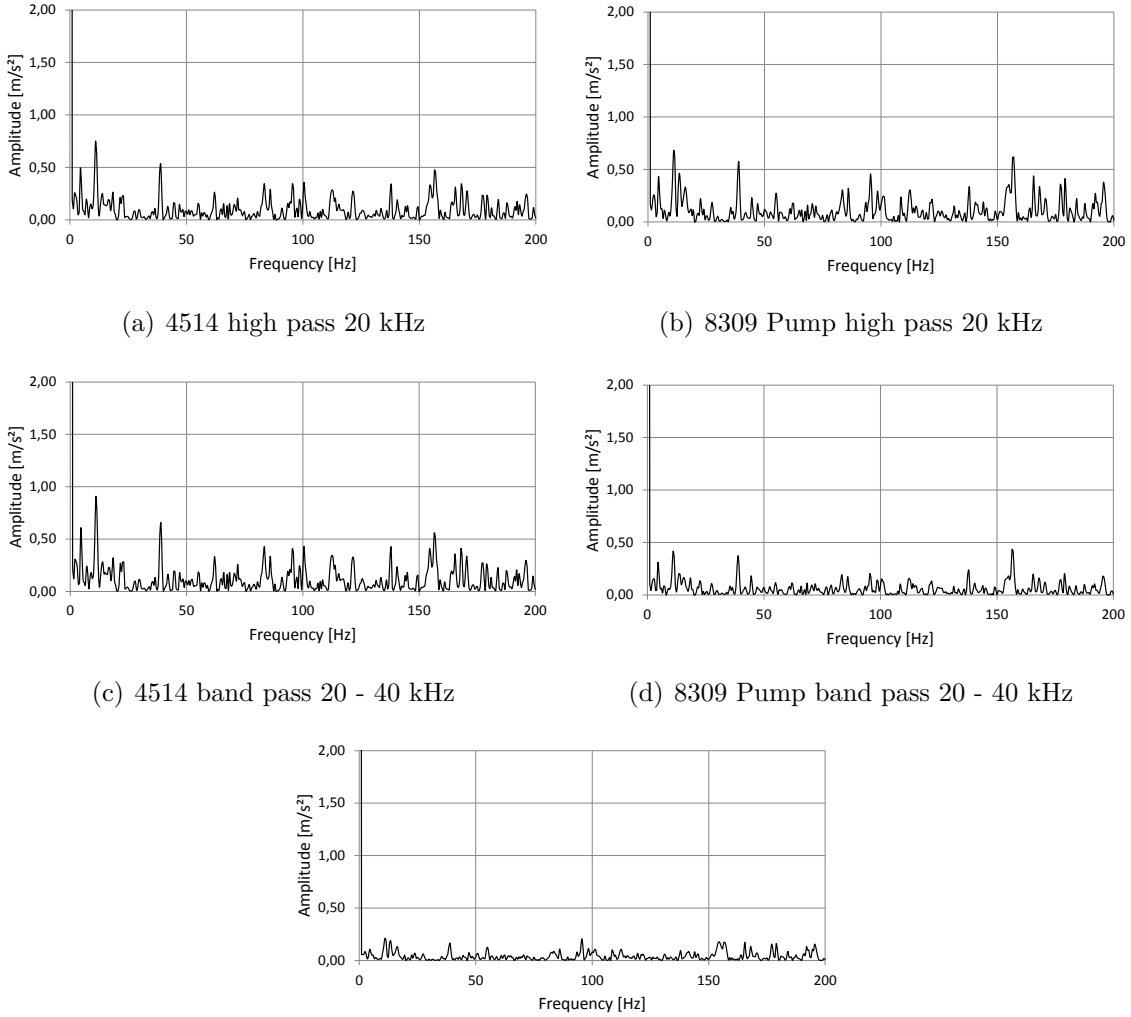

(a) 4514 high pass 20 kHz

(b) 8309 Pump high pass 20 kHz

(c) 4514 band pass 20 - 40 kHz

(d) 8309 Pump band pass 20 - 40 kHz

(e) 8309 Pump band pass 70 - 80 kHz

Figure 5.15: Envelope spectra of the accelerometers on the pump casing at MP 12

The filtering is done with a digital IIR filter. The diagrams show the demodulated signals at MP 12 with the lowest NPSH value and the highest cavitation intensity. The bandwidths were chosen at the appearance of the highest cavitation induced amplitudes in the FFT spectra. It is noticeable, that the biggest peaks appear in each spectra at the same frequencies (11 Hz, 39 Hz, 157 Hz), but there are no remarkable amplitudes in the domain of the blade or shaft passing frequency, which stays in contradiction to the estimations of the envelope detection technique. Demodulations

in other bandwidths did also not reveal any discrete frequencies.

5.4 Measurement Uncertainties

For the completion of the measurements and to prove the reliability of the results, the possible measurement errors and uncertainties are estimated for the calculated and measured parameters. First of all the measured, calculated and assumed parameters, which are necessary to compute the total head, the NPSH values and the blade's incidence angle, and their influencing factors are outlined and summarized in Table 5.2.

Parameters		**measured**	**calc.**	**assumed**	**Influence**
Pressure	p_s, p_p	x			Pressure transducers, Measuring amplifier
Flow rate	Q	x			Flow transducer
Rotational speed	n	x			Speed sensor
Flow velocities	c_s, c_p		x		Flow rate, Pipe diameters d_s, d_p
Vapour pressure	p_v			x	Water temperature
Water density	ρ			x	Water temperature
Gravity	g			x	
Crossflow section	A_1		x		Diameters d_1, d_n from Fig. A.3, simplified calculation
Blade angle	β_{1B}			x	Angle from Fig. A.4
Leakage factor	η_l			x	Sealing

Table 5.2: Measured and assumed parameters

The only parameters which are measured directly, except the vibration measurements, are the pressure on the suction side p_s and on the pressure side p_p, the discharge Q and the rotational speed n of the pump. The other parameters, which are also influencing the results, are calculated from the measured values or assumed from the literature or empirical values.

To reduce uncertainties for the pressure measurements, the whole setup with the transducers and the amplifier was calibrated (see Fig. A.1). The values are mean values of several measurement series to increase the accuracy. To determine the measurement uncertainties due to the test equipment itself, the maximum measurement errors of the pressure transducers, the amplifier and the flow transducer are listed in Appendix A.1. As an example the error values are used to calculate the minimum and maximum pump characteristic with Eq. 5.1 and 5.2, to estimate the reliability of the other measured characteristics and diagrams. The maximum discharge error of ± 0.025 l/s is used to calculate the maximum and minimum flow rate and the flow velocities. The pressure values on the suction and pressure side are calculated with the overall error, consisting of the error for the pressure transducer (± 0.2 %) and the amplifier (± 0.5 %). The results are displayed in Fig. 5.16.

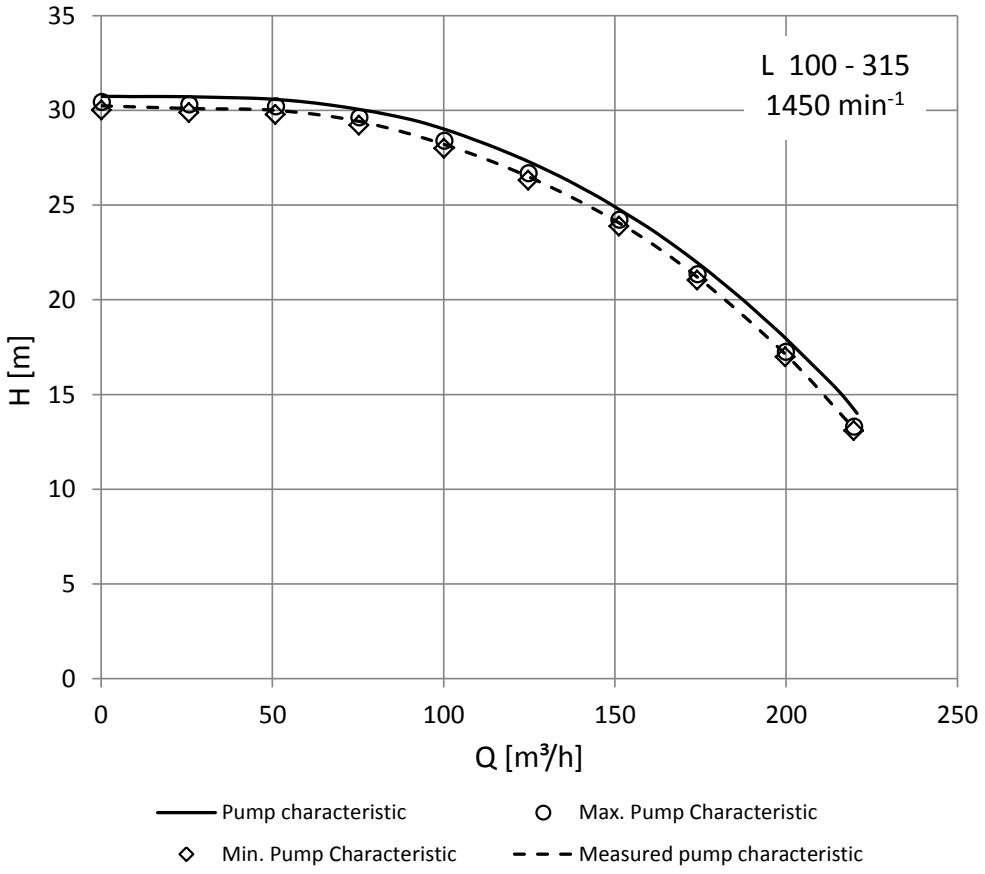

Figure 5.16: Measurement uncertainties for pump characteristic

Due to the low error values of the measuring equipment, the calculated points of the maximum and minimum pump characteristic are very close to the measured characteristic and the error bandwidth caused by uncertainties of the measurement hardware is very narrow. This circumstance indicates also reliable results for the NPSH measurements. It's noticeable, that the pump characteristic from the manufacturer is not in the error range of the measurements, but other uncertainties like pressure losses in the pipe between the pressure transducers and the ring line (see Fig. 4.7(a)) are not considered here and my may expand the error bandwidth.

The uncertainties for the vibration measurements are not so easy to determine, due to the stochastic behaviour of the bubble implosions induced by cavitation. The results in the time and frequency domain illustrate only snapshots and therefore measurement errors are hardly detectable. But for the relevance of the investigations the absolute vibration amplitudes are not so important as the differences between the measuring points and therefore existing measuring inaccuracies can be neglected. However, for the completion of the possible measuring errors, the uncertainties of the 8309 and the 4514 accelerometers are listed in Appendix A.1.

6 Conclusion and Outlook

The implemented measurements and the results shown in chapter 5 have revealed, that cavitation monitoring with the use of piezoelectric acceleration transducers mounted on the pump or turbine casing is a simple method to determine the overall cavitation intensity. The pressure pulsations generated by the implosion of cavitation induced steam bubbles are strong enough to excite noise and vibrations through the fluid in the casing. Even in an operational point, where cavitation is just beginning and vapour bubbles are not or hardly visible, the signals in the time domain display noticeable amplitude peaks. Especially the RMS values of the vibration signals are an appropriate indicator for the cavitation energy. A useful distinction of the cavitation intensity is also possible in the frequency domain as the FFT diagrams of the used accelerometers show. The broad band character of the cavitation noise and it's influence particularly in the higher frequency range require the use of suitable vibration sensors to attain reliable results. Contrary to the time signals and the FFT diagrams the demodulation technique did not lead to the promised success.

One fact that has to be regarded with the employment of piezoelectric accelerometers is their electromagnetic sensitivity. This susceptibility caused problems during the measurement process and distorted the first results so that they were not useful. Only the reduction of the electromagnetic disturbances to a minimum in the measurement environment by the shielding of the pump's power cable solved this problem.

The visual observation of the impeller concerning the amount of cavity exposed to be a helpful method to support the vibration measurements by verifying the cavitation intensity. The appearance of the more aggressive cloud cavitation could also be detected with the camera but the influence on the measured signals could not be verified due to the lack of a high-speed camera. The installation of a visual observation system in a hydraulic machine seems to be a good solution for cavitation detection but this is usually only possible in laboratory models with special visual devices or

prototype pumps or turbines made out of acrylic glass. Cavitation detection systems applied at hydraulic machines in the industrial environment cannot rely on this method but it's the purpose of this development that they get along without it.

The determination of cavitation coefficients like the NPSH value by measuring the static pressure in the inlet of the pump or turbine helps to define the cavitation range, but this requires also the knowledge of the fluid velocity (see Eq. 2.7). While pressure transducers can be easily installed in hydraulic machines, the velocity detection is more difficult to realize especially in large applications. The flow velocity for the measurements was calculated by the discharge rate detected with the flow transducer, which is affordable and easy to mount in smaller pipelines, whereas in hydropower plants other techniques with increased requirements are necessary.

The question which could not be answered during the measurements was the issue of erosion and cavitation damages on the machinery components, especially the runner, in the course of the operation. The pump has been refurbished and all surfaces were powder coated before the test rig was set up, but it was not disassembled again to investigate any erosion rate on the impeller since this has not been the task of this study. Comparing the grid painted on one of the runner blades in Fig. 4.8(b), where the impeller was in new condition and in Fig. 5.5(a), where the pump has been running for several hours in cavitation state, a significant fading of the lines in some parts of the grid is visible. This circumstance leads to the conclusion, that the appearing cavity has an impact on the impeller surface although it can not be proved, that it causes also a damage on the material itself. The idea of measuring the evoked vibrations through the pump's shaft and the backside ball bearing to determine the direct influence of the steam bubble implosions on the runner surface led not to the anticipated success. One reason could be an excessive attenuation between the impeller surface and the sensor, so the cavitation induced vibration signals are covered by the noise of the bearing, or the cavitation impact is too low on the runner. Maybe a shaft-mounted detection system and the measurement of the attenuation as described in [6] could lead to more reliable and useful results.

The determination of the cavitation origins in the pump was also not possible with the sensors mounted on the casing due to the low number of used accelerometers and the associated insufficient spatial resolution. The application of more sensors, especially pressure transducers and hydrophones in the inlet close to the runner perhaps enable a better spatial resolution, but the installation and the complexity of such

systems make it not so affordable for power plant operators.

The general conclusion of this study is, that the overall cavitation intensity and it's increase with a drop of the inlet pressure can be detected with suitable acceleration sensors. One question which remains is, if such high frequency accelerometers can be used in hydropower plants anyway due to the costs, but also because of the altered circumstances between the laboratory model and a large-scale plant. Especially the differences in size, flow rate and rotational speed compared to a big turbine or pump-turbine unit may impose different requirements on the vibration sensors. Therefore one next step to a usable cavitation monitoring system could be investigations on a turbine or pumpturbine test rig or prototype unit. This could probably bring further insights due to similar conditions as found in a hydropower plant and would allow investigations on special turbine components, like guide vane cavitation. Existing studies on prototype machines show confident results: Cencič et al. [12] e.g. performed experiments on a pumpturbine with an installed power in pump mode of 180 MW. The results of the pressure and vibration measurements also show a correlation between a decreasing cavitation number and an increase of the recorded amplitudes. Further investigations in this direction are recommended, to verify and deepen the gained knowledge.

List of Figures

List of Tables

Appendices

A.1 Test Rig and Measurement Equipment

- **E-Motor:**

Manufacturer	ASEA
Type	MBT 180 L
max. Power	22 kW
max. RPM	$1470 min^{-1}$

- **Frequency Converter:**

Manufacturer	Siemens
Type	MIDI MASTER 6SE3123-5DH40
Serial No.	XAF415MD033D

- **Data Acquisition System:**

Manufacturer	Brüel & Kjaer
Type	LAN-XI 3052-A-030
	3-channel input module
Frequency Range	0 - 102.4 kHz
Serial No.	3052-100317
	3052-100405
	3052-100404

- **Pressure Transducer Suction Side:**

Manufacturer	HBM
Type	P6
Serial No.	E67789
Pressure range	0 - 2 bar
	2 bar ≡ 2 mV/V
Max. measurement error	± 0.2 %

- **Pressure Transducer Pressure Side:**

Manufacturer	HBM
Type	P3MA
Serial No.	B96318
Pressure range	0 - 10 bar
	10 bar ≡ 2 mV/V
Max. measurement error	± 0.2 %

- **Measuring Amplifier for Pressure Transducers:**

Manufacturer	HBM
Type	KWS 506 C
Max. measurement error	± 0.5 %

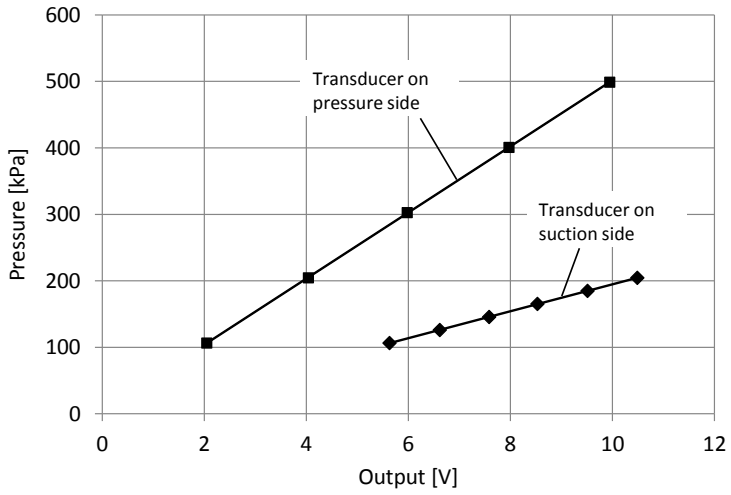

Figure A.1: Calibration diagram for pressure transducers

- **Flow Transducer:**

Manufacturer	Endress + Hauser
Type	Promag 50W1H
Serial No.	EB0A47 19000 C
Current output	0 - 20 mA
	20 mA $\equiv$ 100 l/s
Max. measurement error	$\pm 0.5\ \mu$A $\equiv$ 0.025 l/s

- **High Performance Stroboscope:**

Manufacturer	Philips
Type	PR 9112/00 (Frequency generator)
	PR 9112/10 (Strobe light)
Serial No.	LO - 687

- **Stress Energy Transmitter:**

Manufacturer	Hardy Instruments
Type	HI 5703 ST
Serial No.	1039
Stress Energy Level	0 - 5 or 0 - 10
Output Current	4 - 20 mA
Frequency Range	5 kHz - 60 kHz
Axis Orientation	Any
Supply Voltage	24 vdc volts nominal
	+ 14 vdc to + 36 vdc
Temperature Range	$-40°C to + 85°C$

- **Power Supply for Stress Energy Transmitter:**

Manufacturer	Thurlby Electronics Ltd.
Type	30V-1A PL 310
Serial No.	16726

- **Microphone:**

Manufacturer	Brüel & Kjaer
Type	4954-A-011 (Microphone + Preamplifier)
Serial No.	2704895
Diameter	1/4 inch
Dyn. Range	34 - 164 dB
Freq. Range	3 - 80000 Hz
Sensitivity	2.8 mV/Pa
Pressure Coefficient	-0.007 dB/kPa
Temperature Range	$-20°C to + 100°C$
Input Type	CCLD IEPE

- **Piezoelectric Charge Shock Accelerometer 8309:**

Manufacturer	Brüel & Kjaer
Type	8309
Serial No.	1923232
	30236
Freq. Range	1 - 54000 Hz
Sensitivity	0.04 mV/g
Temperature Range	$-74°C to + 180°C$
Weight	3 g
Electrical Connector	10-32 UNF
Mounting Thread	M5
Resonance Freq.	180 kHz
Uncertainty	1 %

- **Piezoelectric Shear Accelerometer 4514-B-002 :**

Manufacturer	Brüel & Kjaer
Type	4514-B-002
Serial No.	60873
Freq. Range	1 - 12000 Hz
Sensitivity	500 mV/g
Temperature Range	$-51°C to + 100°C$
Weight	8.7 g
Electrical Connector	10-32 UNF
Mounting Thread	10-32 UNF
Resonance Freq.	32 kHz
Uncertainty	1 %

A.2 Radial Pump

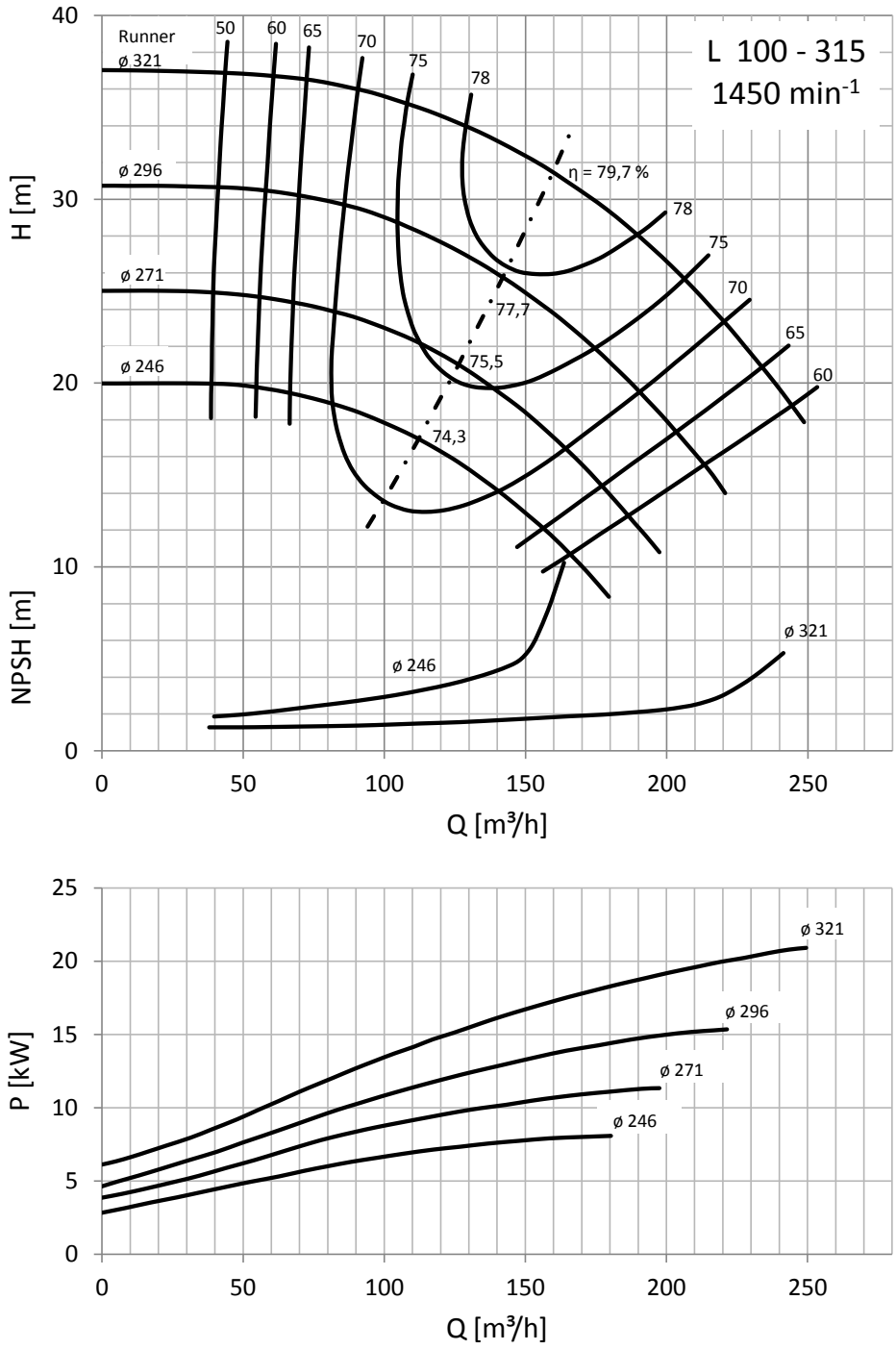

Figure A.2: Pump characteristics from manufacturer

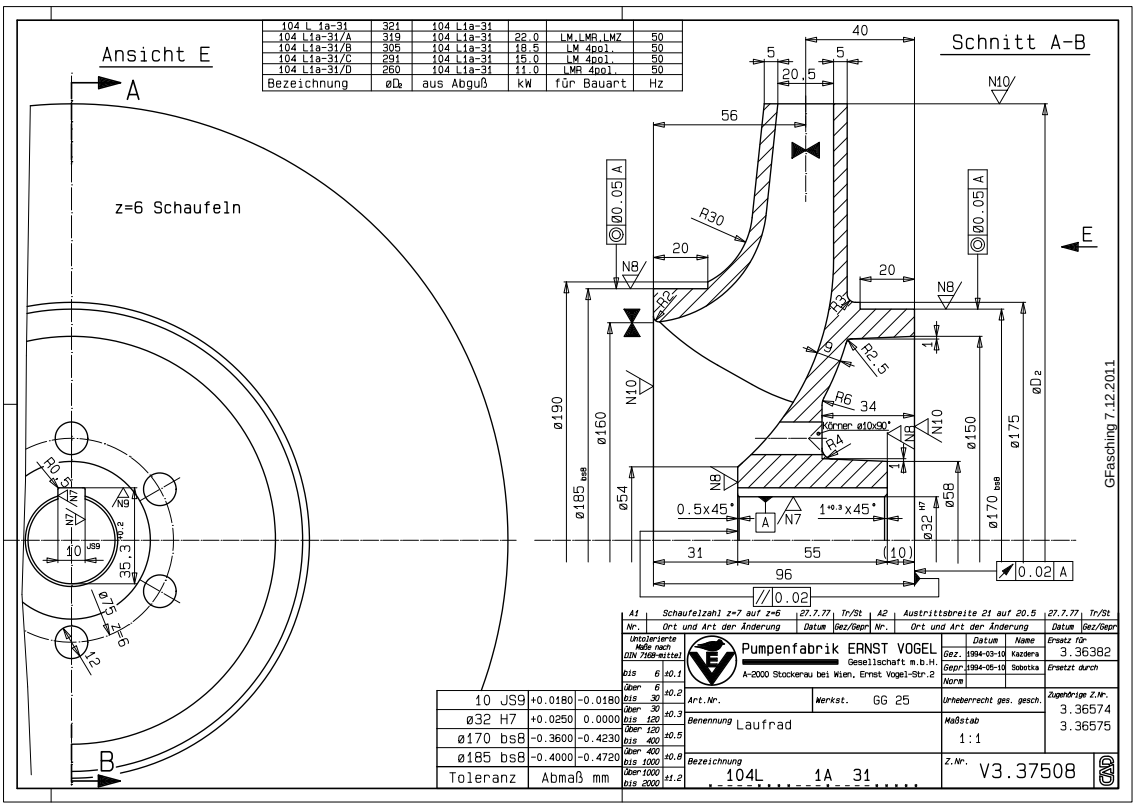

Figure A.3: Detailed runner geometry

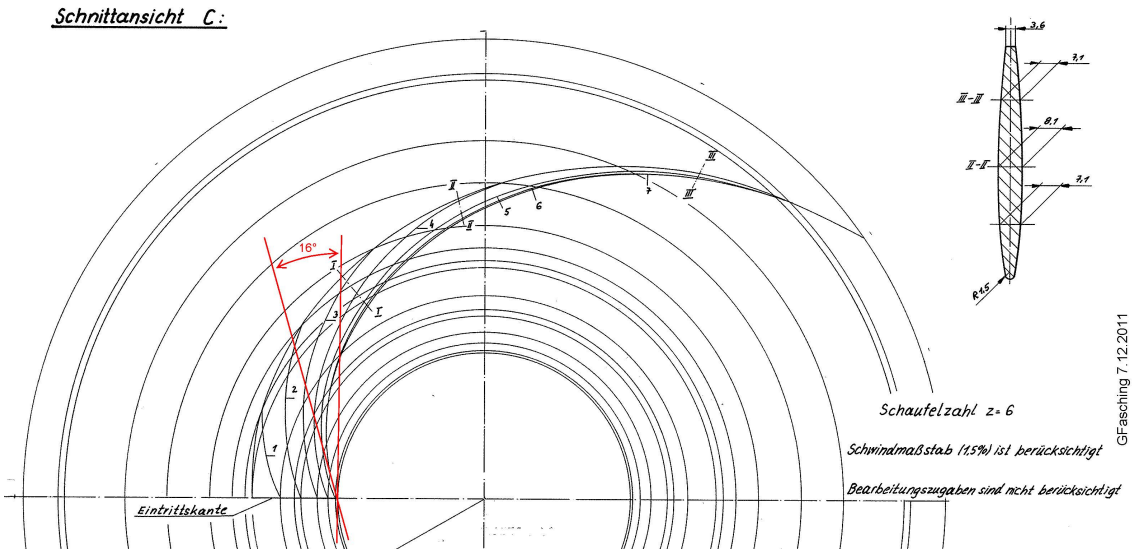

Figure A.4: Impeller section view

A.3 Properties of Water

t °C	p kPa	v' dm^3/kg	v'' m^3/kg	h' kJ/kg	h'' kJ/kg	Δh_v kJ/kg	s' kJ/kg K	s'' kJ/kg K
0,01	0,6117	1,0002	205,99	0,00	2500,9	2500,9	0,0000	9,1555
5	0,8726	1,0001	147,01	21,02	2510,1	2489,1	0,0763	9,0249
10	1,2282	1,0003	106,30	42,02	2519,2	2477,2	0,1511	8,8999
15	1,7058	1,0009	77,875	62,98	2528,4	2465,4	0,2245	8,7804
20	2,3393	1,0018	57,757	83,92	2537,5	2453,6	0,2965	8,6661
25	3,1700	1,0030	43,337	104,84	2546,5	2441,7	0,3672	8,5568
30	4,2470	1,0044	32,878	125,74	2555,6	2429,8	0,4368	8,4521
35	5,6291	1,0060	25,205	146,64	2564,6	2417,9	0,5051	8,3518
40	7,3850	1,0079	19,515	167,54	2573,5	2406,0	0,5724	8,2557
45	9,5951	1,0099	15,252	188,44	2582,5	2394,0	0,6386	8,1634
50	12,352	1,0121	12,027	209,34	2591,3	2382,0	0,7038	8,0749
55	15,762	1,0146	9,564	230,26	2600,1	2369,9	0,7680	7,9899
60	19,947	1,0171	7,667	251,18	2608,9	2357,7	0,8313	7,9082
65	25,042	1,0199	6,194	272,12	2617,5	2345,4	0,8937	7,8297
70	31,201	1,0228	5,040	293,07	2626,1	2333,1	0,9551	7,7541
80	47,415	1,0291	3,4052	335,0	2643,0	2308,0	1,0756	7,6112
90	70,183	1,0360	2,3591	377,0	2659,6	2282,6	1,1929	7,4782
100	101,419	1,0435	1,6718	419,2	2675,6	2256,4	1,3072	7,3542
110	143,38	1,0516	1,2093	461,4	2691,1	2229,7	1,4188	7,2382
120	198,68	1,0603	0,8912	503,8	2706,0	2202,1	1,5279	7,1292

Table A.1: Properties of water [11]

Bibliography

[1] Gülich, J.F.: *Centrifugal Pumps*. 2. Edition. Berlin: Springer 2010

[2] Bauer, C.: *Skriptum zur Vorlesung über Hydraulische Maschinen und Anlagen*. 2. Auflage. Institut für Energietechnik und Thermodynamik. Forschungsbereich Strömungsmaschinen. TU Wien 2010

[3] Bajic, B.: *Multidimensional Diagnostics of Turbine Cavitation*. Journal of Fluids Engineering. Vol. 124. 2002

[4] Bajic, B.: *Vibro-Acoustical Diagnostics of Turbine Cavitation. Examples of Application*. Presented at the HydroVision 2000 Conference, Charlotte, U.S.A. 2000

[5] Bajic, B.: *Cavitation diagnostics and monitoring*. International Water Power & Dam Construction. 2003

[6] Boorsma, A.; Fitzsimmons, P.: *Quantification of Cavitation Impacts with Acoustic Emissions Techniques*. In Proceedings of the 7^{th} International Symposium on Cavitation. Ann Arbor, U.S.A. 2009

[7] Lang, S.; Dimitrov, M.; Pelz, P.F.: *Spatial and Temporal High Resolution Measurement of Bubble Impacts*. In Proceedings of the 8^{th} International Symposium on Cavitation. Singapore 2012

[8] Keil, T.; Pelz, P.F.; Buttenbender, J.: *On the Transition from Sheet to Cloud Cavitation*. In Proceedings of the 8^{th} International Symposium on Cavitation. Singapore 2012

[9] Keil, T.; Pelz, P.F.; Cordes, U.; Ludwig, G.: *Cloud Cavitation and Cavitation Erosion in Convergent Divergent Nozzle*. WIMRC 3^{rd} International Cavitation Forum. Warwick 2011

[10] Li S.C.: *Cavitation of Hydraulic Machinery*. London: Imperial College Press 2001

[11] Baehr, H.D.; Kabelac, S.: *Thermodynamik. Grundlagen und technische Anwendungen*. 13. Edition. Berlin: Springer 2006

[12] Cencič, T.; Hočevar, M.; Širok, B.: *Experimental Investigations of Cavitation in Prototype Turbine*. 21^{st} International Conference Hydroturbo 2012, Brno, Czech Republic